

Radiation Source Localization using a Gamma-ray Camera

Michael Sukyung Lee

August 13, 2018



The Robotics Institute
School of Computer Science
Carnegie Mellon University

Thesis Committee:

William “Red” Whittaker, *Co-Chair*
Nathan Michael, *Co-Chair*
Michael Kaess
Sankalp Arora

*Submitted in partial fulfillment of the requirements
for the degree of Master of Science in Robotics.*

CMU-RI-TR-18-53

Abstract

Radiation source localization is a common and critical task across applications such as nuclear facility decommissioning, radioactive disaster response, and security. Traditional count-based sensors (e.g. Geiger counters) infer range to the source based on the observed number of gamma photons, expected source strength, and assumed intermediate attenuation from the environment. In cluttered 3D settings, such sensors struggle to efficiently disambiguate between symmetries caused by sensor, source, and environment configurations. The recent commercialization of Compton gamma cameras that can not only record counts but also image the direction of incident gamma photons presents new opportunities for efficient radiation mapping and source localization. By leveraging Compton scattering physics, these sensors can obtain bearing measurements to sources independent of strength or attenuation for efficient and accurate source localization.

This three-part thesis develops a full exploration and source localization framework that uses the observations of a gamma camera to efficiently discover and localize sources in cluttered 3D environments. First, an approach to mapping the spatial distribution of radiation in an environment using a gamma camera is presented where observations along the camera's trajectory are incorporated into a consistent voxel grid-based map of source occupancy probabilities. Second, the assumption of a pre-determined trajectory is relaxed and an active source localization framework is developed that greedily selects new waypoints that maximize the Fisher Information provided by the cameras range and bearing observations. As the time required for imaging scales inversely with the square of the distance between the source and camera, proposed active source localization framework is appropriate only within reasonable proximity to a source. Thus, a complementary frontier-based exploration method is finally developed that biases the frontier selection by the observed radiation field gradient to quickly search an environment until a proximal source is detected.

Acknowledgments

I would first like to thank Prof. Red Whittaker for believing in me and providing me with the perfect combination of guidance and space to grow as an independent researcher. You have shown me much grace over the past two years, for which I will always be grateful.

I am indebted to Prof. Nathan Michael for the many hours that he has generously devoted to me first as an undergraduate and now as a Master's student. I would not be where I am today without your mentorship on not only how to engage in research but also how to engage in life purposefully.

And a big thank you to Prof. Michael Kaess and Sankalp Arora for agreeing to be on my committee, sharing valuable feedback, and bearing with me through the winding path of research.

This research would not have been possible without the collaboration of Prof. Zhong He and the Orion Radiation Measurement Lab.

A thank you to Cormac O'Meadhra for challenging, inspiring, and supporting me these past three years. I couldn't have asked for a better friend to go through RISS, a Master's, and now a PhD together with. And a special thanks to Matt Hanczor, my fellow DOE Trainee, with whom I was lucky enough to share this very unique Master's experience with, and Joe Bartels, who helped me get started on this research.

I am grateful to RISLab for fostering such a welcoming research environment and to the Department of Energy for sponsoring this work.

And last, I could not have completed this Master's without the unconditional love and ceaseless prayers of my family. Soli Deo Gloria.

Contents

1	Introduction	1
1.1	Motivation	1
1.2	Thesis Contribution and Outline	3
2	Passive Radiation Source Localization	5
2.1	Fundamentals of Radiation Detection	6
2.2	Related Work	6
2.3	Compton Gamma Camera	9
2.4	Radiation Imaging	11
2.4.1	Sensor Model	11
2.4.2	MLEM Imaging Algorithm	12
2.5	Radiation Mapping	13
2.6	Experiments	15
3	Active Source Localization	21
3.1	Sensor and Motion Models	22
3.1.1	Range and Bearing Sensor Models	22
3.1.2	Motion Model	24
3.2	Greedy Trajectory Optimization	24
3.2.1	Fisher Information Matrix Derivation	24
3.2.2	Control	25
3.3	Parameter Selection	26
3.3.1	Fixed Step Size	26
3.3.2	Adaptive Step Size	27
3.4	Experiments	28
3.4.1	Simulation Environment Development	29
3.4.2	Active Source Localization	29
4	Gradient-biased Frontier Exploration	31
4.1	Related Work	32
4.2	Methodology	33
4.2.1	Weighting of Frontier Voxels	34
4.2.2	Gradient Calculation	37

4.3	Experiments	38
4.3.1	Single Source Localization	40
4.3.2	Multiple Source Localization	44
5	Conclusion	46
5.1	Discussion	46
5.2	Future Work	48
A	Appendix	50
A.1	Sensor Model for Gamma Camera	50
A.2	Maximum Likelihood Expectation Maximization	51

List of Tables

2.1	Passive Source Localization Results	18
3.1	Active Source Localization Results	30
4.1	Frontier Weighting Parameters	34
4.2	Single Source Exploration Results	40
4.3	Multiple Source Exploration Results	44

List of Figures

1.1	Left: Retrieval of nuclear waste stored underground at the Hanford Site in the 1970s and 1980s [5]. Right: Imaging of a radiation hotspot at a reactor in Fukushima using a gamma-ray camera [6].	2
2.1	Top: An unstable radioisotope can decay by emitting an alpha particle, a beta particle, a neutron, a gamma ray, or X-ray. Bottom: Alpha and beta particles are easily stopped by materials such as paper and thin plates, whereas X-rays and gamma rays are stopped by thicker plates with high atomic density. Neutrons are only effectively stopped by hydrogen-rich materials such as water or concrete. [12]	7
2.2	Physics constrains the incident direction of a photon that Compton scatters at two or more interaction locations (P_1, P_2) and energies (E_1, E_2) to lie along a cone along with the axis Ω and opening angle θ . [21]	10
2.3	CdZnTe detector for measuring interaction locations and energy deposition of incident photons [21].	10
2.4	Top: 2D MLEM radiation image of a single source in front of the detector at 45 degrees azimuth and 23 degrees elevation. Bottom: Corresponding 3D MLEM radiation image, where the detector is shown as a blue cube, source is shown as a red sphere. Voxels are colored from yellow to blue, corresponding to the probability being along the source direction.	14
2.5	Collage of experiments being carried out in the small (top left and bottom left) and large (right) laboratory environments with a ground robot equipped with a gamma camera (circled in red).	16
2.6	Test 3: Estimated locations of Ba-133 (purple), Cs-137 (red), Co-60 (orange), and Na-22 (green) as cubes, shown with ground truth source location as spheres, trajectory of robot in red, and spatial map in green.	19
2.7	Test 3: The 20 keV energy windows used to localize sources in test 9 are shown as boxes with the following corresponding colors Ba-133 (purple), Cs-137 (red), Na-22 (green), and Co-60 (orange).	19

2.8	Test 4: Estimated locations of Co-60 (orange) and Na-22 (red) as cubes, with ground truth source location as spheres, trajectory of robot in red, and spatial map in green. The two Cs-137 sources are not shown as they were nearby one another and an insufficient number of photons were observed to resolve them separately via gamma-ray imaging.	20
3.1	Bearing (azimuth Ψ , elevation Φ) and displacement (r_1, r_2, r_3) of sensor with respect to source.	23
3.2	FIM-optimal trajectories using step sizes that vary between 0.3 m to 4 m for a 500 μCi source. Waypoints are marked with circles. As step size is increased, the trajectory takes a progressively direct approach to the source.	27
3.3	Top: Overhead view of FIM-optimal trajectories using adaptive step sizes for sources with strengths from 1 μCi to 500 μCi . Waypoints are marked with circles. Notice that step sizes are adjusted to favor range information for lower strength sources and favor bearing information for higher strength sources. Bottom: Side view.	29
4.1	Flowchart of the proposed exploration framework, which transitions between the exploration (blue) and source localization (green) phases until the environment has been fully explored and no frontiers remain	35
4.2	Selection of frontier cluster: Frontier cells (denoted by the square markers) are grouped into contiguous clusters of the same color, with the mean cell denoted by a green marker. Quadrotor selects the frontier cluster (circled in orange) that is a) close to its current position, b) has the best alignment with the current heading, c) has the best alignment with the perceived gradient direction (indicated by the red arrow), and d) is near measurements made with the highest observed count rate (which is intuitively nearest to the source behind a wall that is circled in blue)	36
4.3	Simulated environment with concrete walls designed to attenuate radiation. The five rooms are labeled A — E.	39
4.4	Relative magnitude of observable count rate for a source in room E, marked by the purple circle. The robot starting location is marked with a yellow triangle.	41
4.5	Representative trajectory for frontier exploration that is biased by the observed radiation gradient.	42
4.6	Representative trajectory for frontier exploration that is not biased by the observed radiation gradient.	42

4.7	Progression of the source localization over multiple imaging dwells (clockwise from top left). The evolving radiation occupancy map that is used for the localization of the source (shown as the purple sphere) is shown as the blue and yellow voxels (in the order of increasing probability of radiation occupancy).	43
4.8	Representative frontier exploration and source localization trajectory for multiple sources.	44
4.9	Close-up of the multiple sources placed in the environment and the trajectories taken by the robot to localize them (in corresponding colors)	45

Chapter 1

Introduction

1.1 Motivation

The discovery of radioactivity by Wilhelm Röntgen, Henri Bequerel, and Curies at the turn of the 20th century ushered in an era of breakthroughs for harnessing this new branch of field of nuclear physics for medicine, power, and weaponry. However, the rapid pace and scale of research and development came with a price. A study conducted by the International Atomic Energy Agency estimated the worldwide legacy of spent nuclear fuel and high level radioactive waste created in the 20th century to be 1,010,000 m³ [1]. To provide an economic and temporal scale to the on-going management of the waste, the United States is projected to spend at least \$240 billion over the next six decades to manage Cold War-era waste alone, much of which still await proper handling at their original processing sites such as Hanford and Savannah River [2].

Despite the already outstanding debt, the present century continues to add to the stockpile of radioactive waste that must be safely managed. The clean-up of the Fukushima Daiichi reactor that underwent a meltdown in March 2011 is projected



Figure 1.1: Left: Retrieval of nuclear waste stored underground at the Hanford Site in the 1970s and 1980s [5]. Right: Imaging of a radiation hotspot at a reactor in Fukushima using a gamma-ray camera [6].

to cost up to \$150 billion USD [3] and carry into the latter half of this century [4]. Furthermore, nuclear power plants across the world are currently producing approximately 34,000 m³ of high level waste annually (which is equivalent to 127 double-decker buses), which must also be constantly cooled, shielded, and monitored [1]. The aforementioned facts confirm that the safe handling of radioactive waste is will remain an immediate and relevant problem in the decades to come. One of the many relevant challenges is the localization and characterization of radioactive sources.

As tissues and organs can suffer damage from sufficient doses of ionizing radiation, humans are limited in or precluded entirely from working in high radiation environments. Such environments present an ideal opportunity for robots to stand in as remote agents that explore, map, and localize the radiation sources contained therein. However, nuclear facilities present many challenges to robotic operation, a reality that has beleaguered efforts to clean up Fukushima to date. Though a number of robots have provided valuable preliminary radiation and visual surveys these past seven years into the cleanup, many others have been lost in the attempts to reach

deeper into the core of the damaged reactors. For example, the tracked Quince robot was abandoned on the 3rd floor of Unit 2 because its communication tether became caught on piping [7]. Additionally, two TEPCO scorpion robots were abandoned after sustaining excess radiation dosage and being blocked by debris respectively [8]. These failures provide insight into the challenges that are common to facilities in the nuclear domain, which are the presence of clutter, radiation, and difficulty of communication.

1.2 Thesis Contribution and Outline

This thesis addresses the aforementioned challenges of localizing radiation sources in nuclear facilities.

Count-based sensors traditionally used for radiation detection (e.g. Geiger-Muller counters and scintillators) can only convey point measurements of field strength [9] and may require extensive observations over space and time to estimate source locations. Even with numerous readings, these sensors may still fail to locate sources in cluttered 3D environments due to symmetries in sensor, source, and environment configurations. The recent commercialization of a sensor called the Compton gamma camera that can record the number of incident gamma photons and image their direction of origin presents new opportunities for efficient radiation mapping and source localization. As a baseline, Chapter 2 proposes a passive source localization approach for a robot equipped with a gamma camera for effective operation in cluttered 3D environments.

The subsequent chapters address the well-known ALARA (As Low as Reasonably Achievable) principle in the nuclear domain that seeks to minimize exposure to radiation and the challenge of communication through the thick, attenuating walls of nuclear facilities. The baseline approach is first extended in Chapter 3 with an active

source localization approach that selects subsequent sensing locations that greedily maximize information gain. Whereas the baseline requires predefined trajectory or teleoperation, this active approach allows the robot to formulate efficiently source localization trajectories for source location hypothesis.

However, the use of the camera may be expensive when it is not near a source and the signal field is weak, as the time required to generate a sufficient image is directly proportional to the strength of the signal field. Chapter 4 thus develops an lightweight exploration algorithm that biases that selection of frontiers with the gradient of radiation intensity that encourages exploration in pursuit of source localization. The efficient, limited autonomy that is developed in Chapters 3 and 4 for source localization both minimizes the dose acquired by the robot and introduces robustness to partial communication failures such as sporadic wireless signal dropout.

Chapter 2

Passive Radiation Source Localization

This chapter establishes a baseline radiation source localization algorithm using the observations of a gamma camera that are passively acquired along a predefined trajectory. After a brief introduction to radiation detection, the use of this sensor class is motivated with a discussion of related works. The following sections detail the sensor model and algorithm that are used to generate a 2D image of the likely source direction. The radiation imaging algorithm is then extended 3D and used to update a radiation occupancy map that is thresholded to estimate locations of sources.

This approach is evaluated with experiments in which a gamma camera was integrated with a ground robot for the localization of multiple point source. All estimated source locations were compared to ground truth, to an average error of 0.26 m in 14×5 m² and 5×4 m² laboratory environments.

2.1 Fundamentals of Radiation Detection

Unstable radioisotopes undergo decay, in which they lose excess atomic mass or energy by emitting particles (alpha, beta, or neutron particles) or energy (x-rays and gamma rays) and become more stable [10]. As gamma rays are electromagnetic waves that typically accompany alpha and beta radiation decay and have greater penetrating power (alpha, beta, and gamma radiation are roughly stopped by a sheet of paper, skin, and lead, respectively), gamma radiation is often used to detect the presence of radioactive sources [11].

Gamma radiation is most commonly detected manually with a point sensor such as a Geiger counter or a scintillator that provide a user with a rate of gamma photons incident the detector. Methods for radiation field mapping and source localization using these count-based sensors have been studied extensively due to their low cost and ubiquity. Two relevant bodies of literature on using the observations of point sensors for radiation mapping and source localization are diverse and briefly survey below, but the ambiguity of point sensor observations forces each work to rely heavily on fundamentally limiting assumptions.

2.2 Related Work

One relevant body of work considers how to spatially interpolate or fit the point observations to a model to yield a radiation field map. Morelande et al. [13] obtain counts from a distributed sensor network and fit a Gaussian Mixture Model over the observed counts. They assume that the number of sources is known and leave model selection for future work. Minamoto et al. [14] build a radiation map of the ground by collecting radiation counts with a handheld dosimeter and finding a maximum a

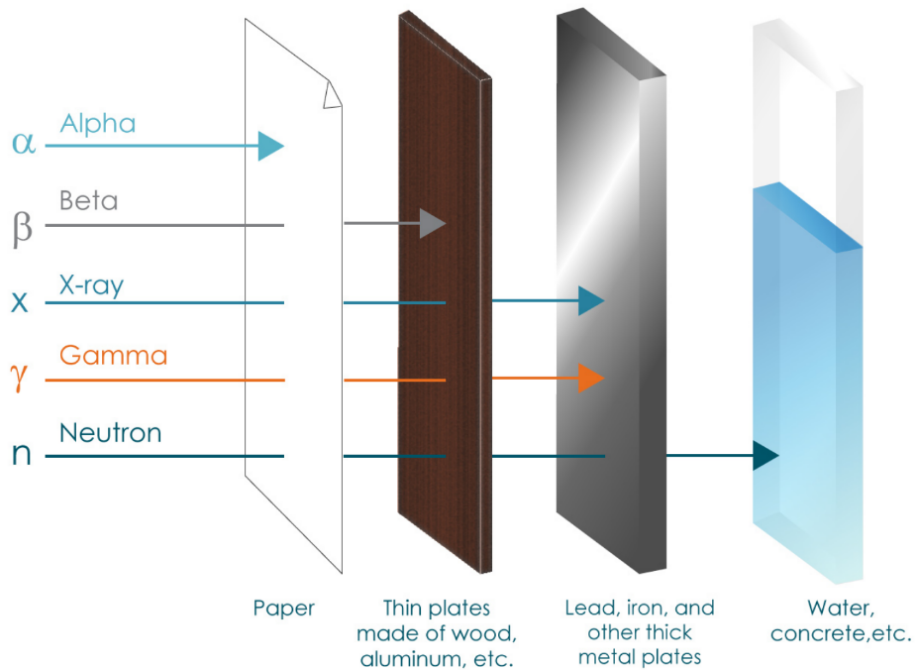
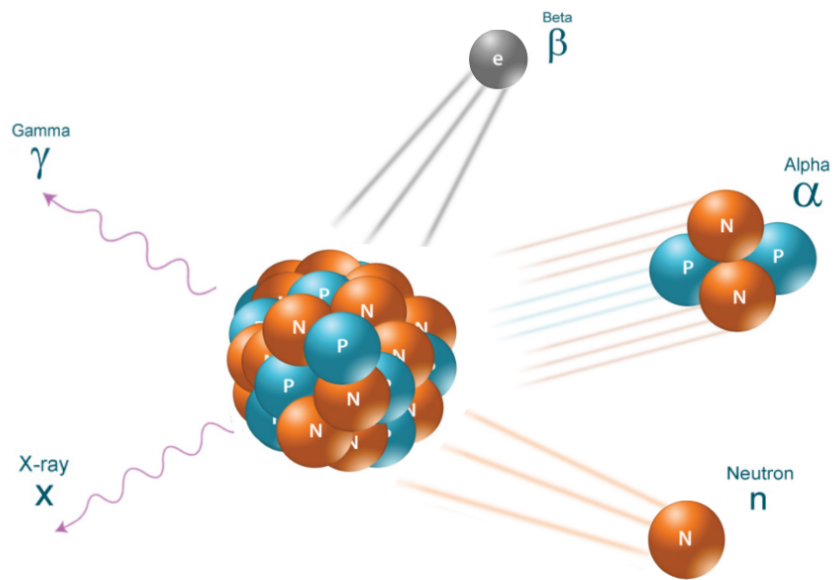


Figure 2.1: Top: An unstable radioisotope can decay by emitting an alpha particle, a beta particle, a neutron, a gamma ray, or X-ray. Bottom: Alpha and beta particles are easily stopped by materials such as paper and thin plates, whereas X-rays and gamma rays are stopped by thicker plates with high atomic density. Neutrons are only effectively stopped by hydrogen-rich materials such as water or concrete. [12]

posteriori estimate over the distribution of point sources using the priors of inverse square law attenuation and Poisson count statistics. The strong priors practically limit this work to simple, open environments in which the inverse square law is valid. Martin et al. [15] fly a UAV equipped with a downward-facing rangefinder and a CZT spectrometer, constructing a 3D topological mesh and an overlay of the observed radiation data under an inverse square law assumption. While the inverse square law assumption is likely valid for aerial radiation mapping, this is likely insufficient for source localization as peaks of intensity measured by a point sensor may not be valid proxies for source locations.

Another relevant body of work for point sensors concerns source localization. Morelande et al. [16] estimates the source locations and intensities using a particle filter and the number of sources using the Bayesian Information Criterion, but it assumes an open, obstacle-free environment. Chin et al. [17] use a hybrid formulation of a particle filter and mean-shift techniques to localize multiple point sources by limiting the sensing range of the nodes of a sensor network and not associating particles to a particular source, allowing groups of nodes to separately localize sources in its neighborhood. Limitations of this method include the need for a densely populated sensor network, the possible difficulty in scaling the particle filter to 3D due to the curse of dimensionality, and the need to manually tune the neighborhood size. Towler et al. [18] use an Archimedian spiral search patterns to gather radiation count measurements from a RC helicopter, discover contour lines, and use a Hough transform to estimate the source positions and intensities for an arbitrary number of point sources. But this work assumes an open field and the Hough transform is based on overlapping circles that depends on the inverse square law. And lastly, Newaz et al. [19] also use a Gaussian mixture model to model the radiation field, and estimate the location and number of sources using variational Bayes inference of Gaussian mixtures. However,

this method is also currently limited to 2D obstacle-free environments.

Though their observations of source proximity prove useful, these count-based sensors ultimately struggle to efficiently disambiguate between symmetries in sensor, source, and environment configurations without limiting assumptions. The recent commercialization of a sensor called the Compton gamma camera that can record the number of incident gamma photons and image their direction of origin presents new opportunities for efficient radiation mapping and source localization. Recent work has shown that a series of bearing readings can be used to iteratively construct a 3D radiation map of a cluttered environment and triangulate to sources [20] using a similar class of sensor used in this paper. This chapter establishes a baseline, passive radiation mapping approach that estimates the location of nearby sources given sensor observations gathered along a set trajectory.

2.3 Compton Gamma Camera

A gamma camera not only provide the count and energy of incident gamma photons but also their direction of origin through Compton imaging. Compton imaging in turn relies on the physics of Compton scattering, in which a photon collides with an electron in its path, deposits a portion of its energy, and deflects in a new direction. Given the incident photon energy, deposited energies, and interaction locations, Compton scattering physics constrains the incident direction to a cone (as shown in Figure 2.2) [21]. As the camera dwells and images at a waypoint, many such Compton cones will accumulate and converge to the direction of the radiation source.

This work uses a Polaris-H sensor, which records the locations of interactions and the deposited energies necessary for Compton imaging using a $2 \times 2 \times 1.5 \text{ cm}^3$ CdZnTe

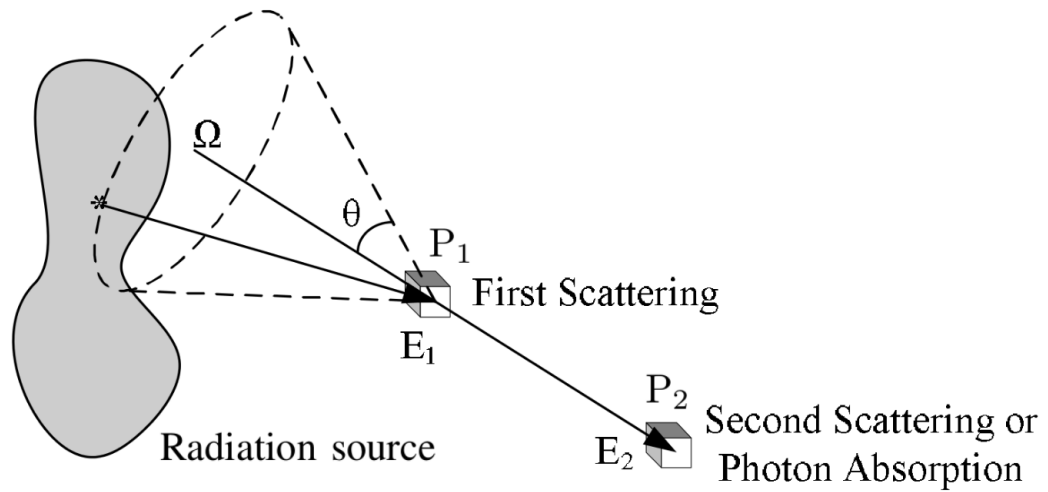


Figure 2.2: Physics constrains the incident direction of a photon that Compton scatters at two or more interaction locations (P_1, P_2) and energies (E_1, E_2) to lie along a cone along with the axis Ω and opening angle θ . [21]

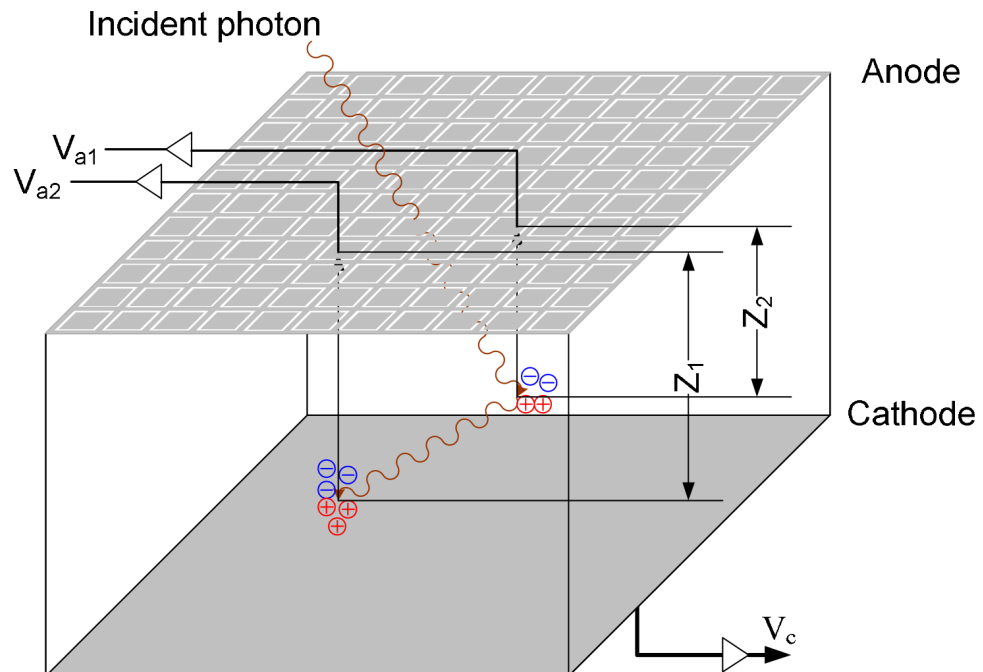


Figure 2.3: CdZnTe detector for measuring interaction locations and energy deposition of incident photons [21].

detector (see Figure 2.3). In what is known as an event, an incident gamma photon may interact m times in the crystal and deposit E_1, E_2, \dots, E_m energies. N events observed by the sensor between time indices $t - 1$ and t will be grouped in sequence in list-mode format as $\mathbf{z}^{(t)} = \{\mathbf{z}_1^{(t)}, \mathbf{z}_2^{(t)}, \dots, \mathbf{z}_N^{(t)}\}$ where $\mathbf{z}_n^{(t)} \in \mathbb{R}^{m \times 4}$, $m \in \mathbb{N}$. Each event is represented as an $m \times 4$ matrix, where each row records the discretized x, y, z coordinates and deposited energy E of an interaction. The ability to detect the energy of an incident photon allows the camera to selectively consider photons with incident energy levels for imaging and analysis. Thus, two isotopes with distinct decay energies can be localized separately without significant crosstalk. The counts and corresponding energies recorded for a later conducted experiment can be found in Figure 2.7, which the peaks corresponding to the decay energies of various isotopes are discernible.

2.4 Radiation Imaging

2.4.1 Sensor Model

The operation of the gamma camera can be described at a high level as a response function that maps radiation source distribution in its environment to corresponding sensor observations. This is captured by the equation below with the source distribution $m_r \in \mathbb{R}^{J \times 1}$, the sensor model $O \in \mathbb{R}^{I \times J}$, and the likelihood of possible sensor observations $\bar{\mathbf{z}} \in \mathbb{R}^{I \times 1}$

$$\bar{\mathbf{z}} = O \cdot m_r \quad (2.1)$$

where the environment is discretized into J voxels, and m_{r_j} is the number of photons emitted from voxel j . I is the space of all possible events (i.e. combinations of possible interaction locations and energies) and $\bar{z}_i \in \bar{\mathbf{z}}$ is the expected number of times the

i th event is observed. To solve for the source distribution, two items are needed: the sensor model and a method of inferring m_r given $\bar{\mathbf{z}}$.

The sensor model o_{ij} is the probability that a photon from voxel j is detected as the event z_i (i.e. $p(\bar{z}_i \geq 1 | m_{r_j} = 1) = o_{ij}$). The analytical sensor model used in this paper is derived in [21], which accounts for the inverse square law radiation, the probabilities of Compton scattering and photoelectric absorption, and the shape of the Compton cone. The full model can be found in Appendix A.1.

2.4.2 MLEM Imaging Algorithm

Once the analytical sensor model has been calculated for each of the observed events \mathbf{z}_n in the list-mode data \mathbf{z} , an iterative imaging algorithm called Maximum Likelihood Expectation Maximization (MLEM) can be applied to infer the source distribution that likely gave rise to the sensor observations [21]. MLEM can be adapted to work in a 2D imaging space to create an image or a 3D imaging space to create a voxel grid-based map. Examples of 2D and 3D MLEM images from the same dwell point are shown in Figure 2.4. While the full algorithm can be found in Appendix A.2, it is briefly described below for qualitative understanding.

Given a set of observed interaction locations and energy depositions of incident photons, the relevant subset of sensor models in O are used to assign a probability to all possible directions of the photons origin. MLEM then iteratively estimates the maximum likelihood source distribution by jointly considering the sensor model and the observed data in an expectation-maximization fashion. The expectation (E) step associates the incident photon of each observed event to the likely direction of origin using the current estimate of the source distribution in the environment. The maximization (M) step then uses the photon-direction association from the expectation

step to compute the next maximum-likelihood estimate of the source distribution. MLEM can be adapted to work in a 2D imaging space to create an image or a 3D imaging space to create a voxel-grid based map.

In contrast to count-based sensors that infer range based on the number of observed counts, source source strength, and intermediate attenuation, gamma cameras can determine the direction of the source without any assumptions on the aforementioned quantities. Radiation images taken at distinct locations can then be used to triangulate the source location. This not only enables operation in a broader class of environments, but also allows the peaks of the radiation maps to be approximated as source locations with fewer assumptions on the source and environment configurations.

2.5 Radiation Mapping

The radiation distribution is modeled as a voxel grid with J voxels that each maintain a probability of containing a source as $\mathbf{m}_p = \{m_{p_1}, m_{p_2}, \dots, m_{p_J}\}$. To build a 3D map from 2D images, each voxel is updated with the occupancy probability of the corresponding 2D image pixel that lies along the same spherical direction.

As MLEM associates a portion of the total number of detected events in $\mathbf{z}^{(t)}$ at time t to each of the J voxels as m_{r_j} (see Eq. 2.1), the following is proposed as the probability of occupancy

$$p(m_{r_j}^{(t)} | \mathbf{z}^{(t)}) = \frac{m_{r_j}^{(t)}}{\max_j(m_{r_j}^{(t)})} = p_j^{(t)} \quad (2.2)$$

If no counts are observed, then $p(m_{r_j}^{(t)} | \mathbf{z}^{(t)}) = 0$.

To incorporate $p_j^{(t)}$ into the map, a threshold is used to first classify the proba-

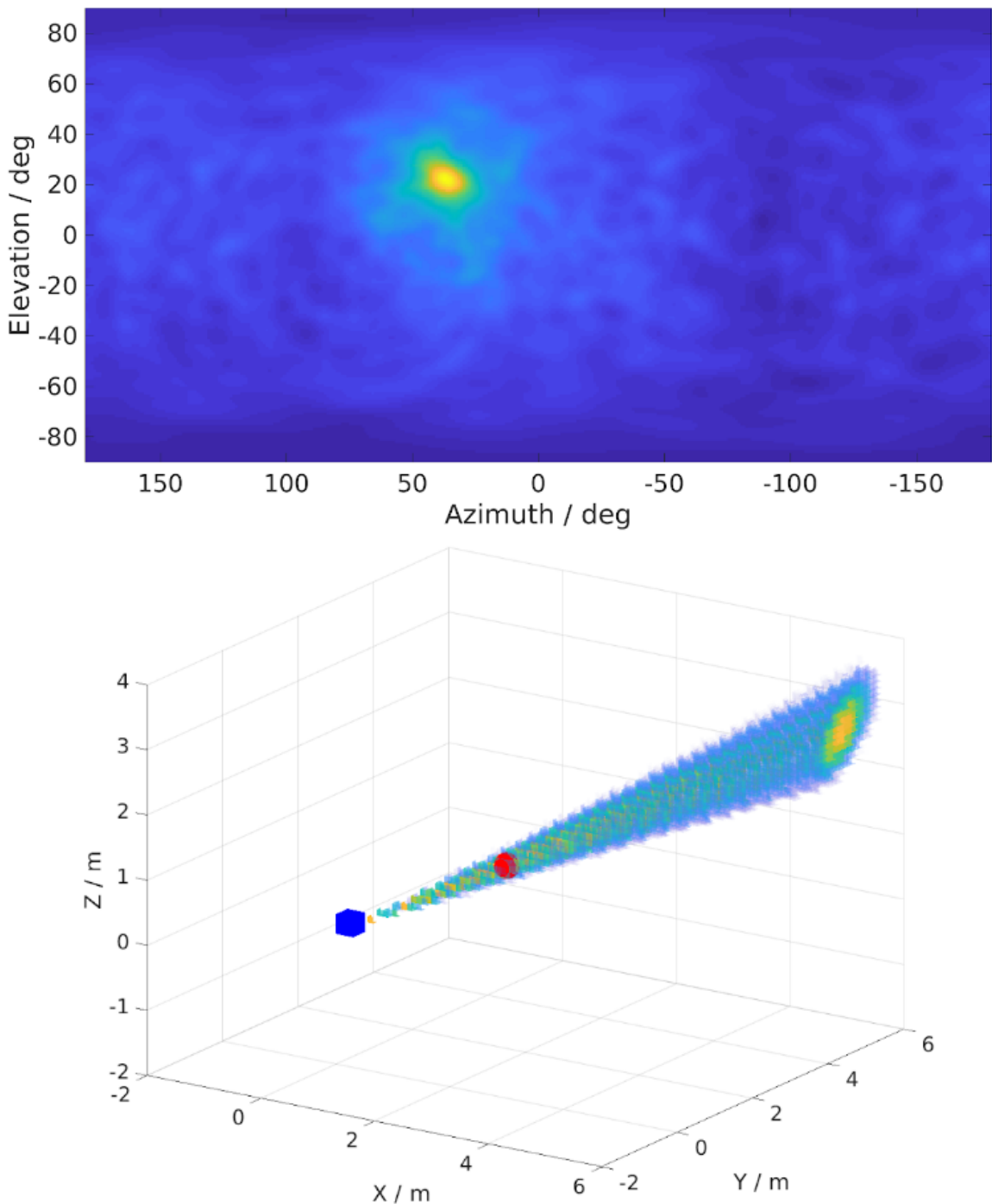


Figure 2.4: Top: 2D MLEM radiation image of a single source in front of the detector at 45 degrees azimuth and 23 degrees elevation. Bottom: Corresponding 3D MLEM radiation image, where the detector is shown as a blue cube, source is shown as a red sphere. Voxels are colored from yellow to blue, corresponding to the probability being along the source direction.

Algorithm 1 Updating Radiation Map

```
1: procedure UPDATERMAP( $\mathbf{m}_p^{(t-1)}, \mathbf{p}^{(t)}, \mathbf{z}^{(1:t)}, \mathbf{T}^{(1:t)}$ )
2:    $counts = length(\mathbf{z}^{(t)})$ 
3:    $total\_counts = \sum_{k=1}^{t-1} length(\mathbf{z}^{(k)})$ 
4:    $\alpha_c = \frac{counts}{total\_counts}$ 
5:    $\alpha_t = \frac{T^{(t)} - T^{(t-1)}}{T^{(t)} - T^{(1)}}$ 
6:   for all  $j$  do
7:     if  $p_{jt} \geq occupancy\_threshold$  then
8:        $m_{pj}^{(t)} = m_{pj}^{(t-1)} + \alpha_c \cdot (p_j^{(t)} - m_{pj}^{(t-1)})$ 
9:     else
10:       $m_{pj}^{(t)} = m_{pj}^{(t-1)} + \alpha_t \cdot (p_j^{(t)} - m_{pj}^{(t-1)})$ 
```

bilities into “positive” and “negative” measurements of source occupancy. “Positive” measurements are scaled by the number of counts received in $\mathbf{z}^{(t)}$ and “negative” measurements are scaled by the duration of $\mathbf{z}^{(t)}$ as counts and time are the units of information for presence and absence of sources, respectively.

A voxel grid-based radiation map m_p is updated with the new probabilities of occupancy $\mathbf{p}^{(t)}$ obtained from the sensor observations $\mathbf{z}^{(t)}$ following Alg. 1. $\mathbf{T}^{1:T}$ denotes the dwell times associated with the sensor observations $\mathbf{z}^{1:t}$. Under the assumptions of no state uncertainty and no measurement uncertainty, the map update simplifies to a moving average update that is computationally light and amenable to real-time performance.

2.6 Experiments

For the first set of experiments, a ground robot was equipped with a Polaris-H gamma camera to follow a predetermined set of dwells and localize multiple point sources of various isotopes and strengths.

Experiments testing the proposed radiation mapping method were conducted in two laboratory environments: a small uncluttered room with $5 \times 4 \text{ m}^2$ meters of open



Figure 2.5: Collage of experiments being carried out in the small (top left and bottom left) and large (right) laboratory environments with a ground robot equipped with a gamma camera (circled in red).

space, and a large and cluttered room approximately $14 \times 6 \text{ m}^2$ in size (see Figure 2.5 for representative images).

A total of 4 tests were performed in the two environments, where each test varied the robot’s trajectory, number of dwells, surrounding point sources, and degree of attenuation. Ground truth measurements of the source locations were recorded to evaluate the accuracy of source locations estimated from LiDAR odometry [22] and MLEM. Details of the four performed experiments can be found in Table 2.1, which compares a baseline, experimental results using the approach described in Section 2.3, and simulation results for validating the simulation environment developed for the following chapter (see Sections 3.4.1 and 3.4.2). A voxel size of 10 cm was used for the radiation map.

Quantitatively, all sources were localized to an average error of 0.26 m across the conducted tests or 0.6% of the environment dimensions. Qualitatively, the estimated and ground truth source locations are placed in the context of the LIDAR map generated by the robot for tests 3 and 4 in Figure 2.6 and Figure 2.8 respectively. As mentioned earlier, the gamma camera is able to localize different isotopes separately by selectively analyzing photons within some window of the energy of interest (i.e. energy windows). The count-energy spectrum of the data collected for test 4 is provided as Figure 2.7, where the peaks corresponding to the decay energies of various isotopes are clearly visible.

The ability to detect the energy of an incident photon allows the camera to selectively consider photons with incident energy levels for imaging and analysis. Thus, two isotopes with distinct decay energies can be localized separately without significant crosstalk. The counts and corresponding energies recorded for a later conducted experiment can be found in Figure 2.7, which the peaks corresponding to the decay energies of various isotopes can be seen.

For comparison with a count-based source localization method, the particle filter and mean-shift-based algorithm from [17] was implemented due to the minimal assumptions theoretically required for the localization of multiple sources. Each particle is a hypothesis of a source location and strength, and by only updating the weights of particles within a defined radius of a measurement location, an arbitrary number of sources can be localized in largely disjoint regions through mean-shift clustering. For all tests, the measurement radius was set to 5 m and the filter was initialized with 1000 particles uniformly sampled throughout the environment with the correct source strength.

As expected, the baseline performed poorly in the large, cluttered environment with an average localization error of 1.931 m as a result of unmodeled attenuation.

Table 2.1: Passive Source Localization Results

Test	Path (number of dwells*)	Source (μCi)	Localization Error (m)		
			Baseline	Experiment	Simulation
1-SM	Straight (6)	Na-22 (61.28)	0.471	0.034	0.034
2-SM [†]	Straight (6)	Na-22 (61.28)	0.528	0.096	0.031
3-SM	Lawnmower (11)	Cs-137 (100)	0.431	0.055	0.053
		Na-22 (61.28)	0.560	0.120	0.037
		Co-60 (48.60)	0.516	0.105	0.089
		Ba-1333 (82.11)	0.970	0.228	0.110
4-LG	Coverage (10)	Cs-137 (27.24)	3.796	0.262	0.063
		Cs-137 (100)	2.608	1.055	1.186
		Na-22 (61.28)	0.769	0.490	0.584
		Co-60 (48.60)	0.552	0.188	0.048

SM and LG denote tests conducted in the small and large environments, respectively.

*All dwells were 1 minute in duration.

[†]Attenuation around the source increased from test 1-SM with a lead brick

The baseline also surprisingly performed poorly in the small, uncluttered environment due to two reasons. The observed count rate is not only dependent on the strength, location, and intermediate attenuation of the source, but also on roughly modeled detector characteristics (e.g. size, intrinsic efficiency) and stochasticity of radioactive decay. Even when all particles were initialized with the correct source strength, the observed count rate rarely matched the expected count rate from particles near the true source location. Second, all radiation measurements were made in a single plane. As a result, particle updates based on the inverse square law could not break the symmetry in the z-axis and struggled to correctly predict the height of the sources.

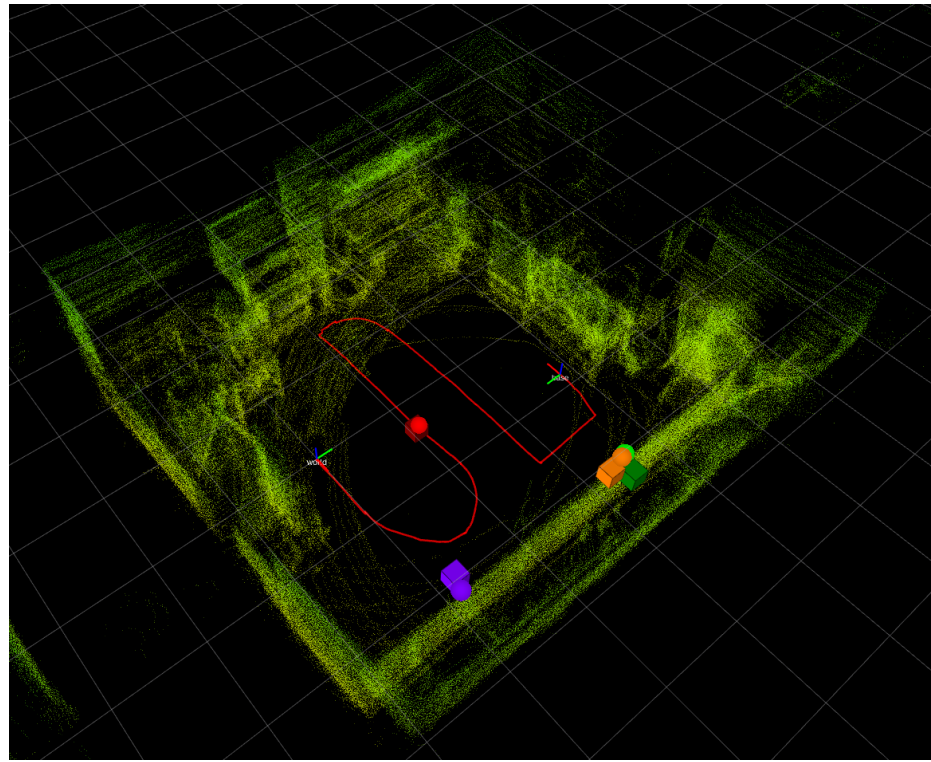


Figure 2.6: Test 3: Estimated locations of Ba-133 (purple), Cs-137 (red), Co-60 (orange), and Na-22 (green) as cubes, shown with ground truth source location as spheres, trajectory of robot in red, and spatial map in green.

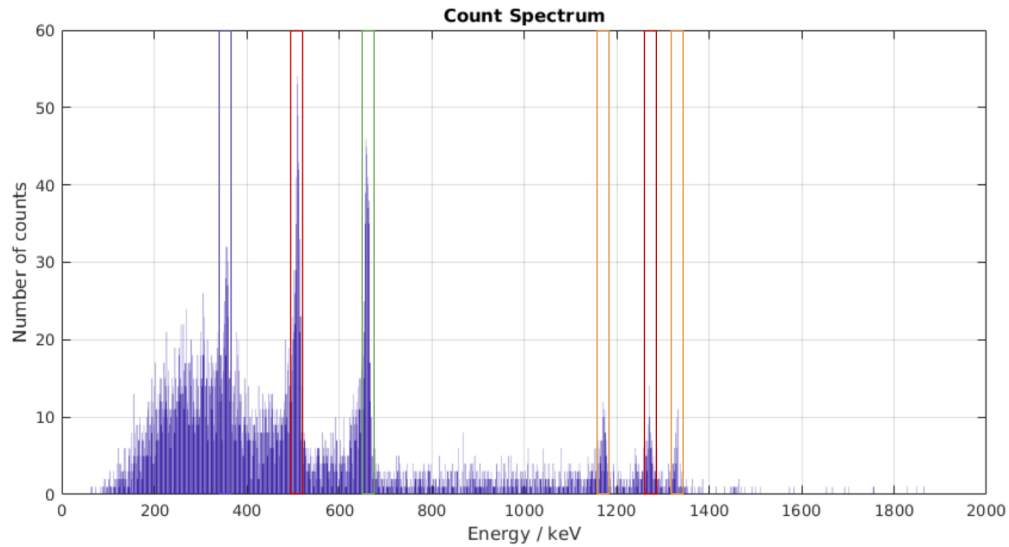


Figure 2.7: Test 3: The 20 keV energy windows used to localize sources in test 9 are shown as boxes with the following corresponding colors Ba-133 (purple), Cs-137 (red), Na-22 (green), and Co-60 (orange).

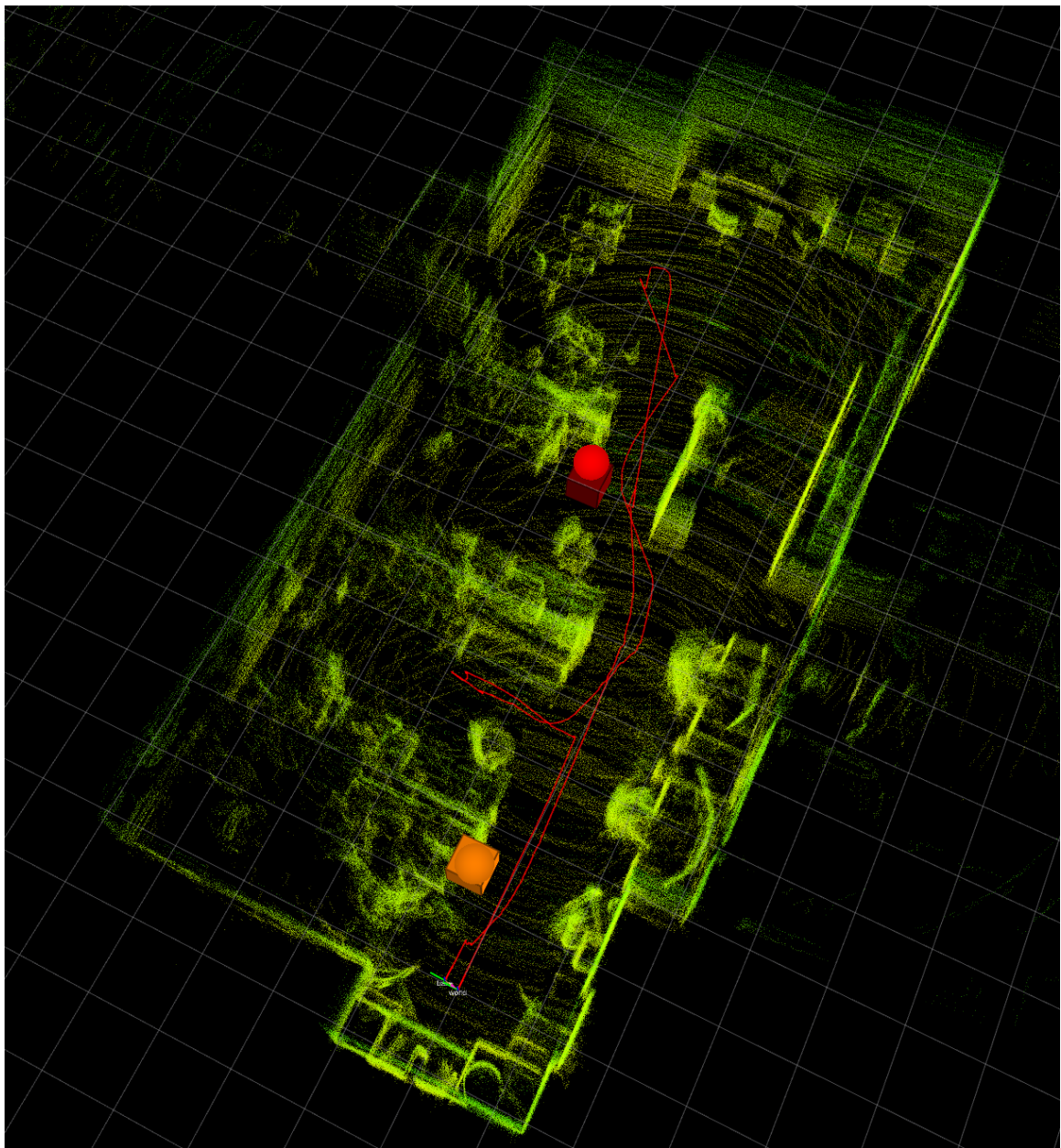


Figure 2.8: Test 4: Estimated locations of Co-60 (orange) and Na-22 (red) as cubes, with ground truth source location as spheres, trajectory of robot in red, and spatial map in green. The two Cs-137 sources are not shown as they were nearby one another and an insufficient number of photons were observed to resolve them separately via gamma-ray imaging.

Chapter 3

Active Source Localization

The baseline source localization algorithm formulated in the previous chapter is passive and thus relies on a predefined trajectory or manual teleoperation. This chapter explores an active source localization method that enables a robot to autonomously follow a path that maximizes the information gain on the estimated source location.

The path that is taken is critical to the efficiency and tractability of localizing a source with a gamma camera. Observations of a gamma camera are range-dependent as a sufficient number of photons must be observed from a nearby source, and bearing-dependent as images provide the direction along which a source lies. Thus an effective source localization trajectory must not only bring a sensor close to the source but also ensure that angular separation of measurements are sufficient for triangulation and observability [23]. A common objective used in trajectory generation is the maximization of a Fisher Information Matrix (FIM) measure [23–27], which broadly measures how informative a random variable (e.g. an observation likelihood) is for estimating an unobservable parameter on which it depends (e.g. a source location). The Fisher Information is also chosen as the objective in this paper for two reasons. First, the Cramer-Rao lower bound proves that the inverse of the Fisher Information

Matrix is the minimum covariance achievable by an unbiased estimator [28]. Second, it has also been shown to yield inward spiraling trajectories [25, 27, 29], that intuitively reduces the distance to the source and allows for bearing observations with sufficient angular separation for triangulation.

This chapter is outlined as follows. Relevant range and bearing sensor models are first formulated, then used to derive an optimal control law that greedily maximizes the range and bearing Fisher information observed for efficient source localization. As the proposed approach is highly sensitive to the step size parameter, an adaptive step size formulation is adopted and tested in simulation. The adaptive step size yields a 27% decrease in the localization time and a 16% decrease in the distances traveled to localize a source in a $15 \times 15 \times 15$ m³ open environment.

3.1 Sensor and Motion Models

3.1.1 Range and Bearing Sensor Models

Let $\mathbf{s} = [s_1, s_2, s_3]^\top \in \mathbb{R}^3$ and $\mathbf{p} = [p_1, p_2, p_3]^\top \in \mathbb{R}^3$ be the source and sensor locations, respectively. The relative position of the sensor is $\mathbf{r} = \mathbf{p} - \mathbf{s}$ as illustrated in Figure 3.1. Observations are defined as random variables range $z_{\mathcal{R}}$ and bearing $z_{\mathcal{B}}$.

The range sensor model considers the probability of observing a given number of photons. Let Q_0 be the known rate of photons incident on the detector 1 m away from the source and Δt be the dwell time of the sensor a distance $\|\mathbf{r}\|$ away from the source. Accounting for the inverse square law of attenuation of radiation, the sensor can be expected to observe the following number photons

$$\mu_{\mathcal{R}}(\mathbf{r}) = \frac{Q_0 \Delta t}{\|\mathbf{r}\|^2} \quad (3.1)$$

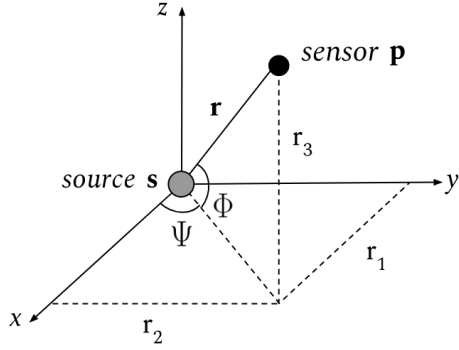


Figure 3.1: Bearing (azimuth Ψ , elevation Φ) and displacement (r_1, r_2, r_3) of sensor with respect to source.

where $\|\cdot\|$ represents the 2-norm.

Though the decay of a source is commonly modeled as Poisson distributed with mean μ if the observation time is much smaller than the source's half-life, a Gaussian distribution with mean and variance μ is a good approximation whenever $\mu > 20$ [9]. As common lab sources between 1 μCi to 100 μCi emit tens of thousands to millions of photons a second, the following Gaussian sensor model is adopted for range

$$p(z_{\mathcal{R}}(\mathbf{r}); \mu_{\mathcal{R}}) \sim \mathcal{N}(\mu_{\mathcal{R}}, \sigma_{\mathcal{R}}^2) \quad (3.2)$$

The bearing to the source provided by a radiation image can be expressed in the source frame with the azimuth and elevation angles Ψ and Φ (see Figure 3.1).

$$\begin{bmatrix} \Psi \\ \Phi \end{bmatrix} = \begin{bmatrix} \tan^{-1}\left(\frac{r_2}{r_1}\right) \\ \tan^{-1}\left(\frac{r_3}{\sqrt{r_1^2 + r_2^2}}\right) \end{bmatrix} \quad (3.3)$$

Dwell times can be varied to ensure that a sufficient number of photons are observed to image the bearing to a source with a desired variance $\sigma_{\mathcal{B}}^2$ (higher observed counts correlate to lower image variance). Assuming an omnidirectional field of view with

minimal directional bias, a Gaussian sensor model is once again assumed. Thus, the same analytical sensor model that was used in [25] is used here.

$$p(z_{\mathcal{B}}; \mu_{\mathcal{B}}, \sigma_{\mathcal{B}}^2) \sim \mathcal{N}(\mu_{\mathcal{B}}, \sigma_{\mathcal{B}}^2) \quad (3.4)$$

3.1.2 Motion Model

A robot that travels a distance d_t along a constant azimuth ψ_t and elevation ϕ_t between waypoints \mathbf{p}_t and \mathbf{p}_{t+1} can be modeled with the following kinematics

$$\mathbf{p}_{t+1} = \mathbf{p}_t + \begin{pmatrix} \cos(\phi_t) \cos(\psi_t) \\ d_t \begin{pmatrix} \cos(\phi_t) \sin(\psi_t) \\ \sin(\phi_t) \end{pmatrix} \end{pmatrix} \quad (3.5)$$

where ψ_t and ϕ_t are defined in a stationary inertial frame.

3.2 Greedy Trajectory Optimization

3.2.1 Fisher Information Matrix Derivation

Candidate waypoints are evaluated based on their expected Fisher Information Matrix (FIM). The FIM of a sensor model $p(z(\mathbf{p})|\mathbf{s})$ at a waypoint \mathbf{p} about the source location \mathbf{s} is defined as follows

$$FIM(\mathbf{s}, \mathbf{p}) = \mathbb{E}\{[\nabla_{\mathbf{s}} \ln p(z(\mathbf{p})|\mathbf{s})][\nabla_{\mathbf{s}} \ln p(z(\mathbf{p})|\mathbf{s})]^{\top}\} \quad (3.6)$$

where ∇ is the gradient operator. The FIM for an N-dimensional Gaussian with constant variance, $X \sim N(\bar{\mu}(\theta), \Sigma)$, that is parameterized by K-dimensional parameter

vector $\theta = [\theta_1, \dots, \theta_K]^\top$, has the following analytical form for the element in the i th row and j th column (where $1 \leq i, j \leq K$)

$$FIM_{(i,j)} = \frac{\partial \bar{\mu}}{\partial \theta_i} \Sigma^{-1} \frac{\partial \bar{\mu}}{\partial \theta_j} \quad (3.7)$$

Adapting Eq. 3.7 for the range sensor model and the source parameter vector \mathbf{s} evaluates to

$$\begin{aligned} FIM_{\mathcal{R}}(\mathbf{r}) &= \frac{4Q_0 \Delta t}{(r_1^2 + r_2^2 + r_3^2)^3} \begin{bmatrix} r_1^2 & r_1 r_2 & r_1 r_3 \\ r_1 r_2 & r_2^2 & r_2 r_3 \\ r_1 r_3 & r_2 r_3 & r_3^2 \end{bmatrix} \\ &= 4Q_0 \Delta t \frac{\mathbf{r} \mathbf{r}^\top}{(\mathbf{r}^\top \mathbf{r})^3} \end{aligned} \quad (3.8)$$

Similarly, adapting Eq. 3.7 for the bearing sensor model evaluates to

$$\begin{aligned} FIM_{\mathcal{B}}(\mathbf{r}) &= \frac{1}{\sigma_{\mathcal{B}}^2} \left(\begin{bmatrix} \frac{r_2^2}{(r_1^2 + r_2^2)^2} & \frac{-r_1 r_2}{(r_1^2 + r_2^2)^2} & 0 \\ \frac{-r_1 r_2}{(r_1^2 + r_2^2)^2} & \frac{r_1^2}{(r_1^2 + r_2^2)^2} & 0 \\ 0 & 0 & 0 \end{bmatrix} + \begin{bmatrix} \frac{r_1^2 r_3^2}{(r_1^2 + r_2^2 + r_3^2)(r_1^2 + r_2^2)} & \frac{r_1 r_2 r_3^2}{(r_1^2 + r_2^2 + r_3^2)(r_1^2 + r_2^2)} & \frac{-r_1 r_3}{r_1^2 + r_2^2 + r_3^2} \\ \frac{r_1 r_2 r_3^2}{(r_1^2 + r_2^2 + r_3^2)(r_1^2 + r_2^2)} & \frac{r_2^2 r_3^2}{(r_1^2 + r_2^2 + r_3^2)(r_1^2 + r_2^2)} & \frac{-r_2 r_3}{r_1^2 + r_2^2 + r_3^2} \\ \frac{-r_1 r_3}{r_1^2 + r_2^2 + r_3^2} & \frac{-r_2 r_3}{r_1^2 + r_2^2 + r_3^2} & \frac{r_1^2 + r_2^2}{r_1^2 + r_2^2 + r_3^2} \end{bmatrix} \right) \\ &= \frac{1}{\sigma_{\mathcal{B}}^2} \left(\tilde{\mathbf{r}} \tilde{\mathbf{r}}^\top + \frac{\check{\mathbf{r}} \check{\mathbf{r}}^\top \oslash \hat{\mathbf{r}}^\top \hat{\mathbf{r}}}{\mathbf{r}^\top \mathbf{r}} \right) \end{aligned} \quad (3.9)$$

where $\tilde{\mathbf{r}} = [r_2, -r_1, 0]^\top$, $\check{\mathbf{r}} = [r_1 r_3, r_2 r_3, -\sqrt{r_1^2 + r_2^2}]^\top$, $\hat{\mathbf{r}} = [\sqrt{r_1^2 + r_2^2}, \sqrt{r_1^2 + r_2^2}, 1]$, and \oslash denotes the Hadamard division.

3.2.2 Control

Scalar measures of $FIM_{\mathcal{R}}$ and $FIM_{\mathcal{B}}$ that encourage measurements that approach the source and obtain sufficient angular separation for triangulation are sought, which

leads to the following objective function

$$J(\psi, \phi, d) = \ln \text{tr}(FIM_{\mathcal{R}}) - \ln \text{tr}(FIM_{\mathcal{B}}^{-1}) \quad (3.10)$$

The trace taken of $FIM_{\mathcal{R}}$ (T-optimality) is sensitive only to the gross distance to the source and favors the shortest path to the source. However, such a motion collapses a 3D source localization problem into a 1D line search and leaves some source parameters unobservable. The trace of the inverse FIM (A-optimality) complements by minimizing the average variance of the source parameter estimates and encouraging spiraling motions that render all source parameters observable [25]. Finally, the logs help scale the two measures, whose operating range can vary in orders of magnitude across a single mission due to the inverse square law decay and optimization of near-singular matrices of potential waypoints.

The controller greedily maximizes the proposed objective over a single step of a given step size d_t to determine the next dwell location. This takes the form of an optimization over the heading angles ψ_t, ϕ_t

$$[\psi^*, \phi^*] = \underset{\psi, \phi}{\text{argmax}} J(\psi, \phi, d) \quad (3.11)$$

3.3 Parameter Selection

3.3.1 Fixed Step Size

The step size between waypoints is a key parameter that implicitly determines the relative scaling between $FIM_{\mathcal{R}}$ and $FIM_{\mathcal{B}}$ and consequently the shape of the trajectory. Eq. 3.8 and 3.9 reveal that $FIM_{\mathcal{R}}$ and $FIM_{\mathcal{B}}$ roughly scale linearly with the cross distance (xx^\top) and with the third and second order of the squared distance

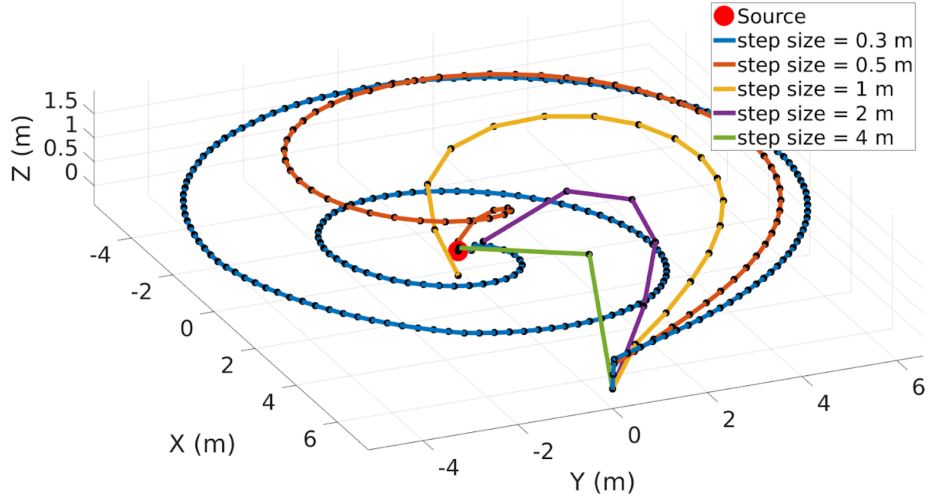


Figure 3.2: FIM-optimal trajectories using step sizes that vary between 0.3 m to 4 m for a $500 \mu\text{Ci}$ source. Waypoints are marked with circles. As step size is increased, the trajectory takes a progressively direct approach to the source.

$(x^\top x)$ respectively. As noted in [29], the squared terms draw the sensor directly to the source while the cross terms induce a circling behavior. This can be observed in Figure 3.2 where incremental increases in step size yield allow the squared terms to dominate and assert a more direct approach toward the source. Although the relative weighting between $FIM_{\mathcal{R}}$ and $FIM_{\mathcal{B}}$ can be modified by a tradeoff parameter to shape the trajectories, none was used in this paper.

3.3.2 Adaptive Step Size

Heuristics such as the step size and planning horizons are commonly set to an empirical value that yields good performance [29–32]. Some works, however, adapt the heuristics online, such as [33, 34], where the planning horizon is increased until sufficient information is gained for robustness to local minima.

Drawing a parallel between the magnitude of gradients and information gain, this paper takes an approach similar to [35] to adaptively determine the step size. The

referenced gradient-based source seeking algorithm scales the step size inversely with the magnitude of the gradient. Their step size is modeled after the common form for gradient gain coefficients used in the literature [36, 37] which takes the following form

$$a_t = \frac{a}{(t + 1 + \xi)^\alpha}, \quad t = 0, 1, 2, \dots \quad (3.12)$$

where a is a constant, ξ is the inertia against monotonically decreasing step sizes over time, and a_t is the step size at time step t . α is set to 0.602 as recommended in [37]. Like [35], this paper adapts Eq. 3.12 by allowing the constant a to change with the observed information at time t . Differences in the referenced and the proposed approach include an exponential scaling to account for log taken in Eq. 3.10, and separate step factors $\eta_{\mathcal{R}}$ and $\eta_{\mathcal{B}}$ for scaling the range and bearing step sizes that are tuned manually.

$$d_t^{\mathcal{R}} = \frac{(1 + \xi)^\alpha \exp(-\eta_{\mathcal{R}} \ln \text{tr}(FIM_{\mathcal{R}}))}{(t + 1 + \xi)^\alpha}, \quad t = 0, 1, 2, \dots \quad (3.13)$$

$$d_t^{\mathcal{B}} = \frac{(1 + \xi)^\alpha \exp(-\eta_{\mathcal{B}} \ln \text{tr}(FIM_{\mathcal{B}}^{-1}))}{(t + 1 + \xi)^\alpha}, \quad t = 0, 1, 2, \dots \quad (3.14)$$

Trajectories generated with adaptive step sizes that balance the objectives of proximity and triangulation are shown in Figure 4.4.

3.4 Experiments

This set of experiments examine the source localization efficiency and accuracy of the developed control law across a range static and adaptive step sizes in simulation.

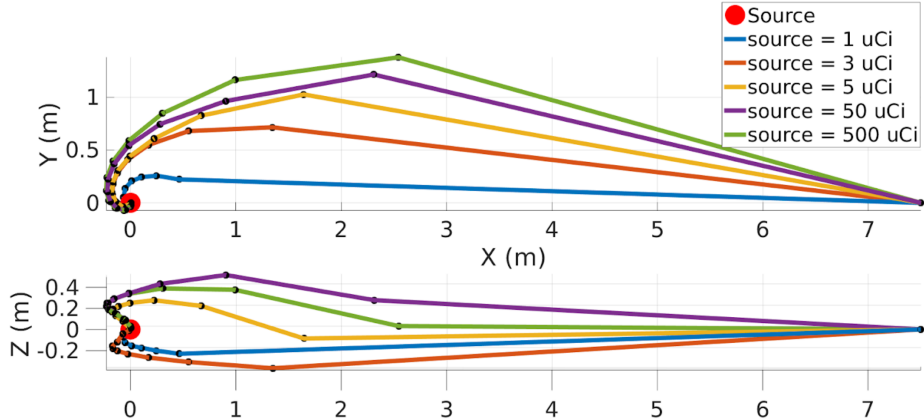


Figure 3.3: Top: Overhead view of FIM-optimal trajectories using adaptive step sizes for sources with strengths from $1 \mu\text{Ci}$ to $500 \mu\text{Ci}$. Waypoints are marked with circles. Notice that step sizes are adjusted to favor range information for lower strength sources and favor bearing information for higher strength sources. Bottom: Side view.

3.4.1 Simulation Environment Development

A radiation simulation environment that models the interaction between gamma photons and the Polaris-H sensor was developed in GEANT4, a particle physics simulator developed by CERN. The system response of the camera were also modeled following the analysis of [38] for higher simulation fidelity. To validate the developed environment for the purposes of active source localization, the experiments of Section 2.6 were replicated with the same source distribution, dwell times, and dwell points. The comparable simulation results are provided in Table 2.1.

3.4.2 Active Source Localization

The proposed control law and adaptive step size is evaluated statistically by running a large number of randomized source localization tests. The robot is initialized in a random location in a $15 \times 15 \times 15 \text{ m}^3$ space to localize a $500 \mu\text{Ci}$ Cs-137 source placed at the center. 100 tests are run for each of the following step sizes: 1 m, 2 m, 4 m, and

Table 3.1: Active Source Localization Results

Step Sizes	1 m	2 m	4 m	Adaptive
Rate of success	53%	95%	90%	100%
Number of Waypoints*	17.32 ± 1.02	11.65 ± 0.48	10.29 ± 0.62	11.88 ± 0.94
Localization error, cm*	1.40 ± 3.79	0.62 ± 3.03	2.59 ± 6.09	2.5 ± 5.8
Total dwell time, min*	12.47 ± 6.07	10.36 ± 6.47	9.38 ± 5.67	6.88 ± 3.50
Distance traveled, m*	8.16 ± 3.79	10.65 ± 4.64	18.58 ± 11.67	6.87 ± 3.39

*Values are provided as $[\mu \pm \sigma]$

adaptive. The following parameters were used for the adaptive step size: $\eta_R = 0.50$, $\eta_B = 0.15$, $\xi = 50$, $\alpha = 0.602$, and the map voxels are set to 10 cm. Each test is carried out until the variance of the source localization estimate falls below 0.15 m or 30 minutes have elapsed. Note that the robot dwells at each waypoint until the number of photons necessary for sufficient resolution of source direction has been observed. And as the proposed FIM-based trajectory optimization requires an initial source location estimate, the second waypoint is always taken perpendicular to the source direction provided by the first waypoint’s image. This triangulation maneuver yields an initial source location estimate that can be used in the optimization of subsequent dwells. The results of the experiments can be found in Table 3.1.

A fixed step size of 1 m often fails to approach the source quickly enough to localize before the 30-minute time limit. A fixed size of 4 m obtains comparable localization error but at the cost of a high distance traveled as it cannot decrease the step size as it nears and circles the source. Though, a fixed size of 2 m has the lowest source localization error, the adaptive approach has the lowest dwell time and the shortest distance traveled for a comparable source localization error. The adaptive step size’s ability to quickly approach the source then circle the source with smaller step sizes also allows it to have a 100% completion rate.

Chapter 4

Gradient-biased Frontier Exploration

The previous chapter developed an active source localization framework that greedily selects waypoints that maximize the Fisher Information provided by a gamma camera’s range and bearing observations of a source for efficient localization. An implicit assumption made by this framework is that the sensor is already sufficiently near a source such that the dwell time necessary to obtain a resolved image is reasonable. This chapter relaxes that assumption and explores how a robot can efficiently explore an environment to discover the presence of a source and subsequently engage in localization.

A frontier-based exploration component that allows the robot to quickly search an unknown environment for sufficient source signal is developed to complement the source localization framework developed in Chapters 2 and 3. The selection of frontiers is biased by the count and gradient information observed by the gamma camera, and thus tailored to the task of source localization. The approach is evaluated in a simulated cluttered environment under single and multiple source localization tasks,

and is shown to cut the distance traveled by up to 50% in the scenarios considered and successfully localize sources amongst clutter.

4.1 Related Work

Methods of exploration in robotics can largely be divided into two camps: frontier-based and sampling-based. Frontier-based methods make the assumption that the most amount of information can be gained by sequentially visiting the boundaries between known and unknown space (i.e. frontiers), and research largely focuses on selecting the next best frontier given a set of objectives (e.g. minimize time taken, energy expended, etc). Sampling-based methods also seek future states that will maximize the information gain, unlike frontier-based methods they operate in the configuration space of the robot. As the previous chapter details a method for selecting optimal poses for localizing a source that's within proximity, and we also assume the use of omnidirectional spatial and radiation sensors, the computationally light frontier exploration methods that aim to quickly uncover the unknown map is favored here.

The original work on frontier exploration by Yamauchi [39] used the simple, intuitive heuristic of selecting the closest frontier as the destination at each time step. The bulk of the follow-up works have varied the way that frontier are selected, for example by selecting frontiers that minimize the change in velocity for rapid exploration [40], favoring frontiers with many identifiable features for localization and mapping [41], and choosing frontiers that promise a large expected information gain after performing an sensing action for efficient exploration [42] (note that the last two methods are a hybrid of frontier and sampling-based methods as they sample the best configuration near frontiers).

The objective function used to weight frontiers can be application-specific as well. For radio frequency (RF) source localization, [43] biases the frontier selection by the frontier’s alignment with the currently observed RF signal gradient and the magnitude of nearby RF measurements. Drawing a parallel between RF and gamma radiation source localization, this particular work is adapted for radiation source localization for this chapter.

4.2 Methodology

The proposed combined framework consists of two phases as Figure 4.1 shows: frontier exploration and source localization. Before the robot is in the vicinity of a source and observes a sufficiently high count rate, it engages in frontier exploration in a receding horizon fashion. First, the laser rangefinder measurement of the current robot pose is processed to update the list of free, occupied, and frontier voxels in occupancy grid map maintained for exploration. Under the assumption that the value of neighboring frontiers will be similar during selection, frontiers are clustered into groups and only the median frontier of each group is evaluated. The best frontier is selected based on a weighted sum of metrics (detailed in Section 4.2.1), and the robot moves a fixed distance toward that frontier and records the number of observed counts. If the count is sufficiently high, then the robot transitions to the source localization phase and optimizes for waypoints that maximize the Fisher Information provided by the gamma camera measurements. The robot remains in this phase until the source is localized to within a desired variance (which was set to be 10 cm in this chapter). If the observed count is too low, then the robot processes the new laser rangefinder measurement and evaluates the next frontier to head toward. This process is repeated until no more frontiers remain. The next two sections detail the frontier

selection process and estimation of the gradient using count measurements.

4.2.1 Weighting of Frontier Voxels

The median voxel of all frontier clusters are evaluated based on a weighted sum of four factors. The first two are radiation-agnostic and include the distance from the robot’s position and alignment with the robot’s heading. Selecting the closest frontier with minimal deviation from the current heading minimizes travel time, energy, and accumulating error in a robot’s state estimate [41]. The last two factors are radiation-dependent and are alignment with the calculated gradient and the average count (which are determined using the N closest points to the current location). Frontiers that best align with the observed gradient are most likely to lie in the direction of the source. Twigg et al. [43] also found that using both the gradient and counts in selecting frontiers led to faster source localization compared to using just one of the two factors, as the estimation of the gradient can become ill-conditioned when measurements are colinear, and the count factor can complement in such instances if the measurements are spaced sufficiently apart. The weights are selected to vary the four factors within the same order of magnitude ($10^0 - 10^2$), which can be found in the Table 4.3. An instance of frontier selection is captured in Figure 4.2.

Table 4.1: Frontier Weighting Parameters

Distance (m)	Rotational deviation (rad)	Gradient deviation (rad)	Average count per second
Operational range	0 - 30	0 - 3.14	0 - 500 [†]
Weight	10	50	100

[†]Stated operational range is representative of the exploration phase, which sees fewer counts than the source localization phase

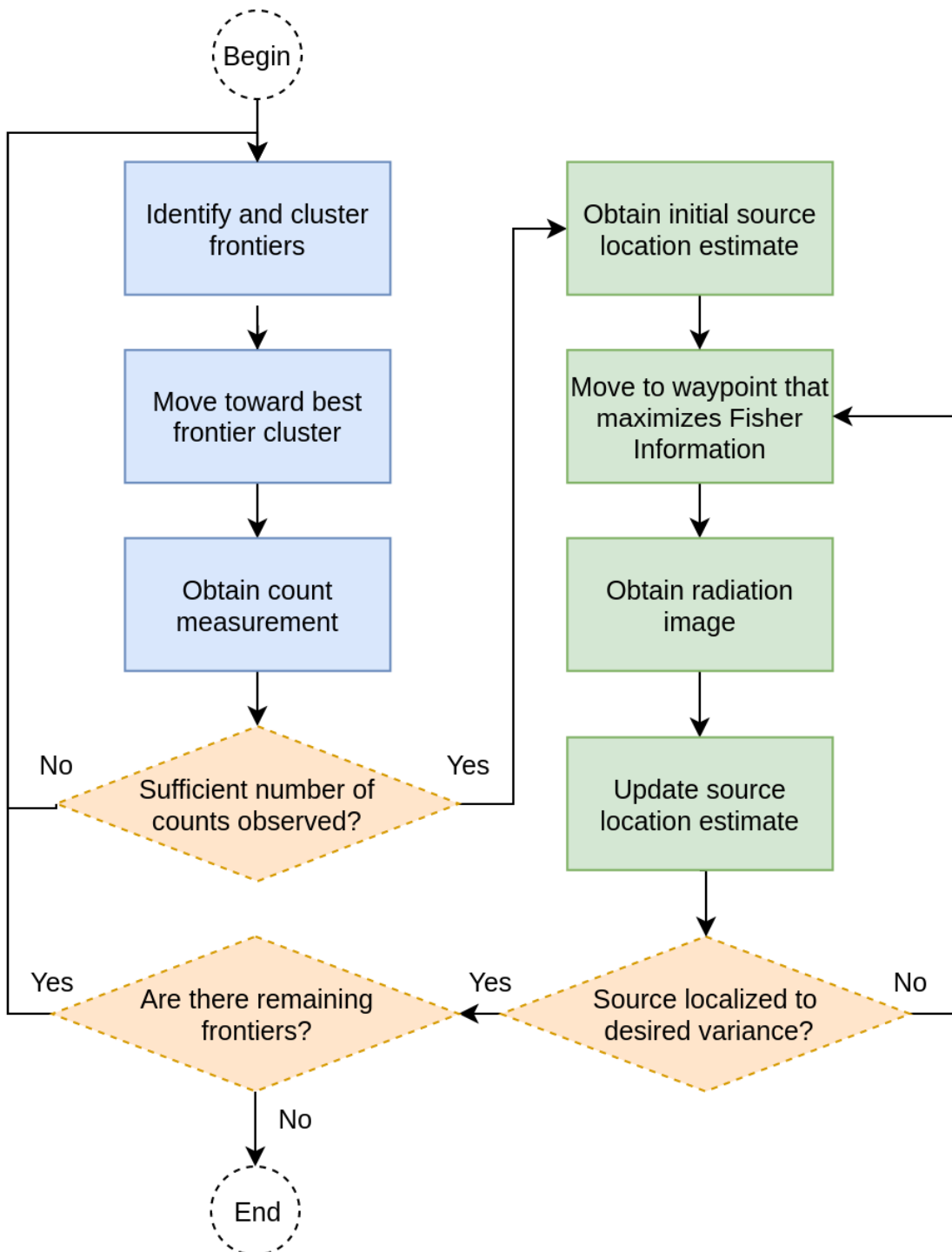


Figure 4.1: Flowchart of the proposed exploration framework, which transitions between the exploration (blue) and source localization (green) phases until the environment has been fully explored and no frontiers remain

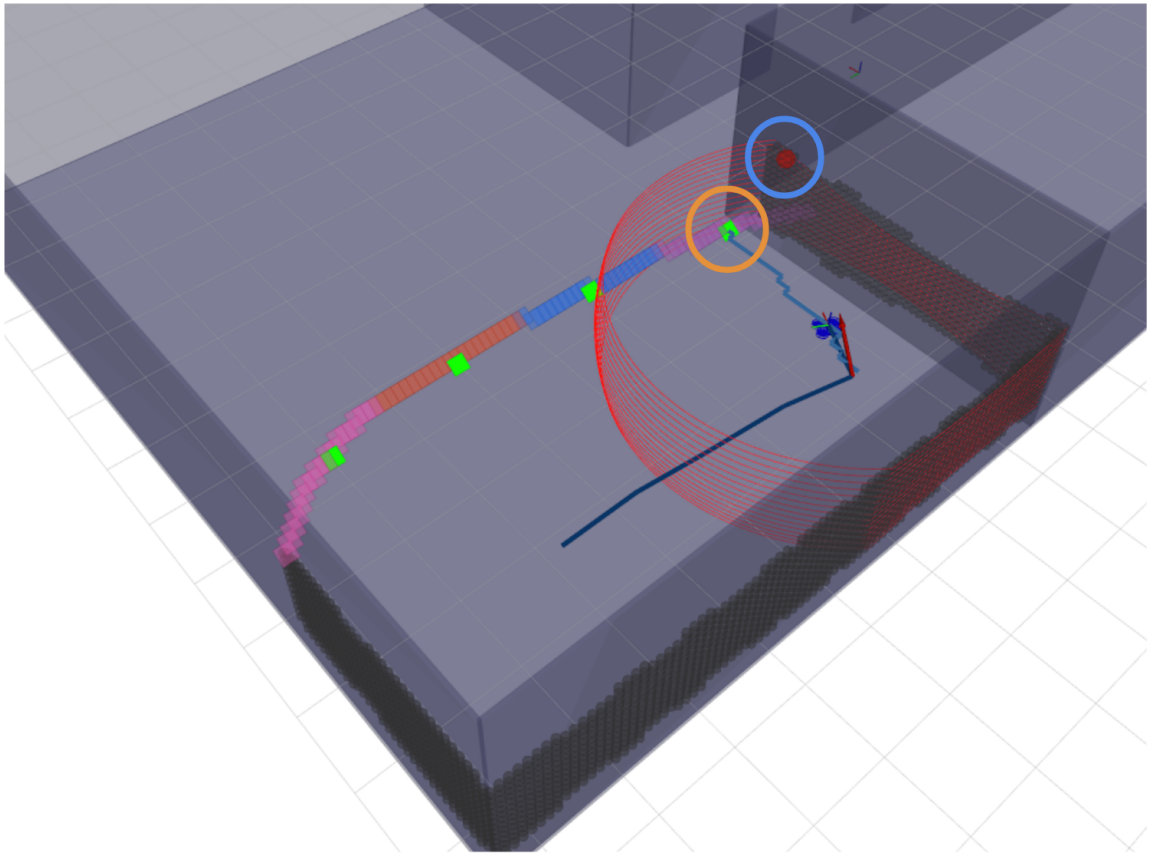


Figure 4.2: Selection of frontier cluster: Frontier cells (denoted by the square markers) are grouped into contiguous clusters of the same color, with the mean cell denoted by a green marker. Quadrotor selects the frontier cluster (circled in orange) that is a) close to its current position, b) has the best alignment with the current heading, c) has the best alignment with the perceived gradient direction (indicated by the red arrow), and d) is near measurements made with the highest observed count rate (which is intuitively nearest to the source behind a wall that is circled in blue)

4.2.2 Gradient Calculation

The following method for calculating the gradient using least-squares estimation can be found in the appendix of [43] and is reiterated here for completeness.

Let $Z_n \in \mathbb{N}$ be the count measurement made at location $(X_{1,n}, X_{2,n}, X_{3,n}) \in \mathbb{R}^3$.

First, center each of the N measurements so that

$$\sum_n X_{1,n} = \sum_n X_{2,n} = \sum_n X_{3,n} = 0 \quad (4.1)$$

Of interest is the gradient $(\beta_1, \beta_2, \beta_3) = \beta$, which describes how the expected count measurement varies in the space centered around the mean measurement location. The relationship between the gradient, measurement location, and the expected measurement value can be described mathematically as follows

$$\mathbf{X}\beta = \mathbf{Z} \quad (4.2)$$

where $\mathbf{X} \in \mathbb{R}^{N \times 3}$ and $\mathbf{Z} \in \mathbb{N}^{N \times 1}$ are the vectorized form of the N measurements and $\beta \in \mathbb{R}^{3 \times 1}$ is the gradient.

Performing the least squares estimation of β amounts to

$$\beta = (\mathbf{X}^\top \mathbf{X})^{-1} \mathbf{X}^\top \mathbf{Z} \quad (4.3)$$

The gradient in the azimuth and elevation spherical directions, β_{azi}, β_{ele} can then be calculated as follows

$$\begin{aligned} \beta_{azi} &= \tan^{-1} \left(\frac{\beta_2}{\beta_1} \right) \\ \beta_{ele} &= \tan^{-1} \left(\frac{\beta_3}{\sqrt{\beta_2^2 + \beta_1^2}} \right) \end{aligned} \quad (4.4)$$

This chapter considers single and multi-source localization, but assumes that there

is only one source of each isotope. Therefore, count measurements made along various energy lines are stored in separate k-d trees specific to each isotope. Gradients are then determined for each of the isotopes using N of the closest measurement points to the robot's current location, where N was set to 10 for the following experiments.

4.3 Experiments

Experiments a single source were carried out in simulation to compare the efficiency of the proposed gradient-biased frontier exploration method for rapid source localization against a baseline frontier exploration method that only accounts for radiation-agnostic factors in the frontier selection. Experiments for multiple source localization were carried out to demonstrate the robustness of the proposed approach to varied source locations in a cluttered environment.

The $12 \times 24 \times 3$ m³ simulation environment was designed to emulate a nuclear facility with 5 rooms divided by concrete walls (see Figure 4.3). For computational efficiency, lower source strengths and 5 cm-thick walls were used, but the results provided here are transferable to environments with stronger source strengths and thicker walls. To calculate the expected attenuation from the walls, the following formula is used

$$I = I_0 e^{-\mu x} \quad (4.5)$$

where I is the attenuated intensity, I_0 is the original intensity, μ is the linear attenuation coefficient that characterizes the attenuation capacity of the medium, and x is the distance to be traveled by the photons through the medium. With concrete's linear attenuation coefficient of 0.1975/cm for 600 keV photons (which is roughly half of the decay energy range of the sources used in this paper), photons directly incident

the 5 cm wall will at least be attenuated to 0.3725 the original intensity. Photons entering at an oblique angle will travel a greater distance through the wall and will thus be further attenuated.

Qualitatively, the formula was used to estimate the gradient field resulting from the source, attenuation from the walls for each of the four source locations, and the inverse square fall off of radiation. Because of the inverse square law, a logarithmic scaling was used for color.

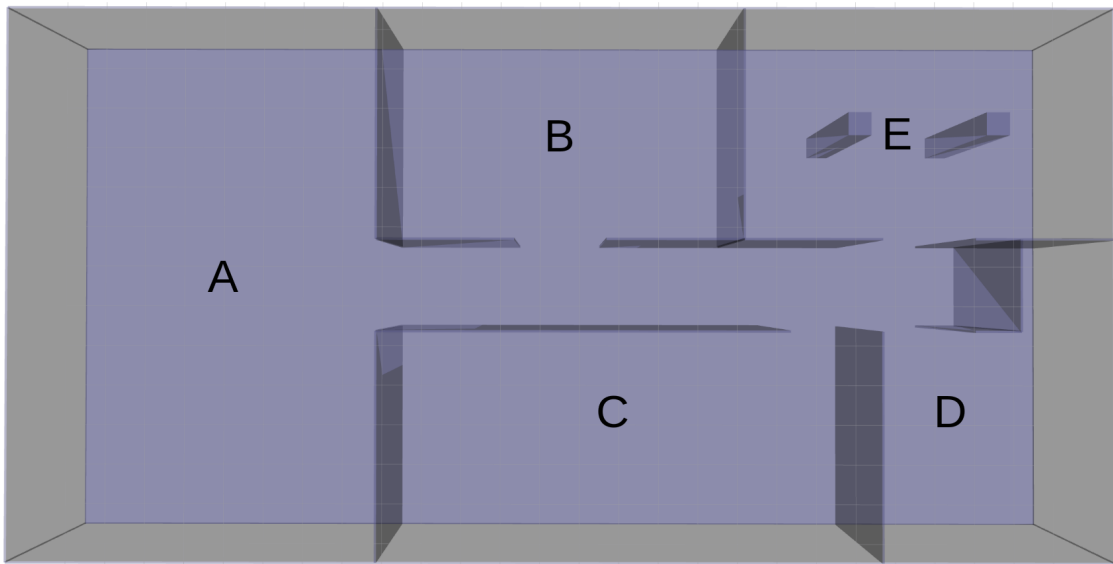


Figure 4.3: Simulated environment with concrete walls designed to attenuate radiation. The five rooms are labeled A — E.

With a comparatively low ceiling, proximal sources would be detected regardless of their height. Thus the exploration was carried out in 2D, where at each time step 2D frontiers would be extracted as a slice of the 3D occupancy grid map at the current height of the robot. The FIM-optimal trajectory that was developed in Chapter 3 was however allowed to follow 3D trajectories for full observability of the source x, y, and z coordinates.

4.3.1 Single Source Localization

Under the hypothesis that radiation-dependent factors in the frontier selection would enable more efficient exploration for source localization, the proposed exploration method that uses all four factors was compared against a baseline that only takes into account the distance and alignment with the robot's heading.

In all experimental runs, the robot was initialized in the bottom left corner of the map to follow the combined exploration framework until the 300 mCi Na-22 source in room E was localized. Ten trials were conducted, and the distance to source localization, localization accuracy, and total dwell time used in imaging for both methods were recorded. The corresponding result statistics can be found in Table 4.2. The transition between the exploration and source localization phases was set to occur at 3,000 counts per second.

To understand how the radiation-dependent factors would influence the exploration trajectory, an qualitative map of the relative flux (i.e. count rate per unit area) throughout the environment was created using the expected attenuation from the walls and the fall off of radiation with the square of the distance (see Figure 4.4). Note that the robot does not have access to this ground truth flux map, and must generate it on the fly using the observed count rates and the least-squares gradient estimation outlined in Section 4.2.2.

Table 4.2: Single Source Exploration Results

	Baseline Exploration	Gradient-biased Exploration
Distance Traveled, m*	83.96 ± 0.45	42.06 ± 2.70
Localization Error, m*	0.02 ± 0.04	0.02 ± 0.05
Total Dwell Time, s*	2.85 ± 0.13	2.17 ± 0.41

*Values are provided as $[\mu \pm \sigma]$

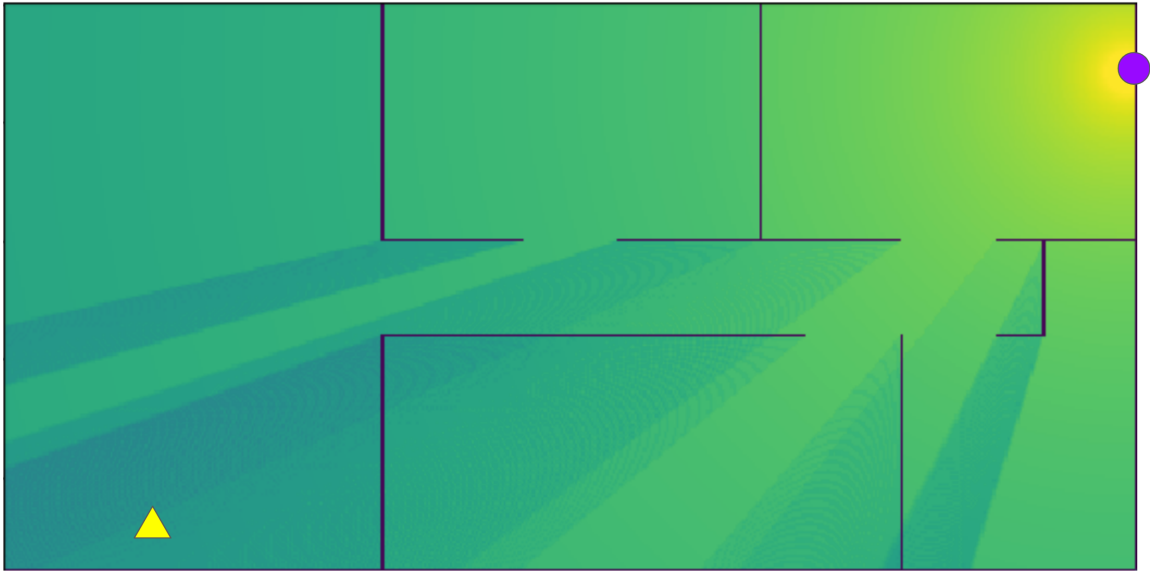


Figure 4.4: Relative magnitude of observable count rate for a source in room E, marked by the purple circle. The robot starting location is marked with a yellow triangle.

As expected, taking into account radiation information in the form of gradients and counts led to a more focused search for the source. Figure 4.5 shows how the gradient leads the robot quickly out of room A and into the center corridor, and away from rooms C and D. However, the gradient reasonably leads the robot into room B as it lies along the path from the starting location to the source location. As Figure 4.6 shows, the baseline fully explores room A as well as room D nearly doubling the total traveled distance. Note that in this figure, the source localization trajectory has carried the robot to a different height, updating the list of 2D frontiers such that it seemingly crosses the path history from an overhead view.

For visual understanding of the progression of the source localization via triangulation, Figure 4.7 shows how the source location estimate evolves over subsequent imaging dwells.

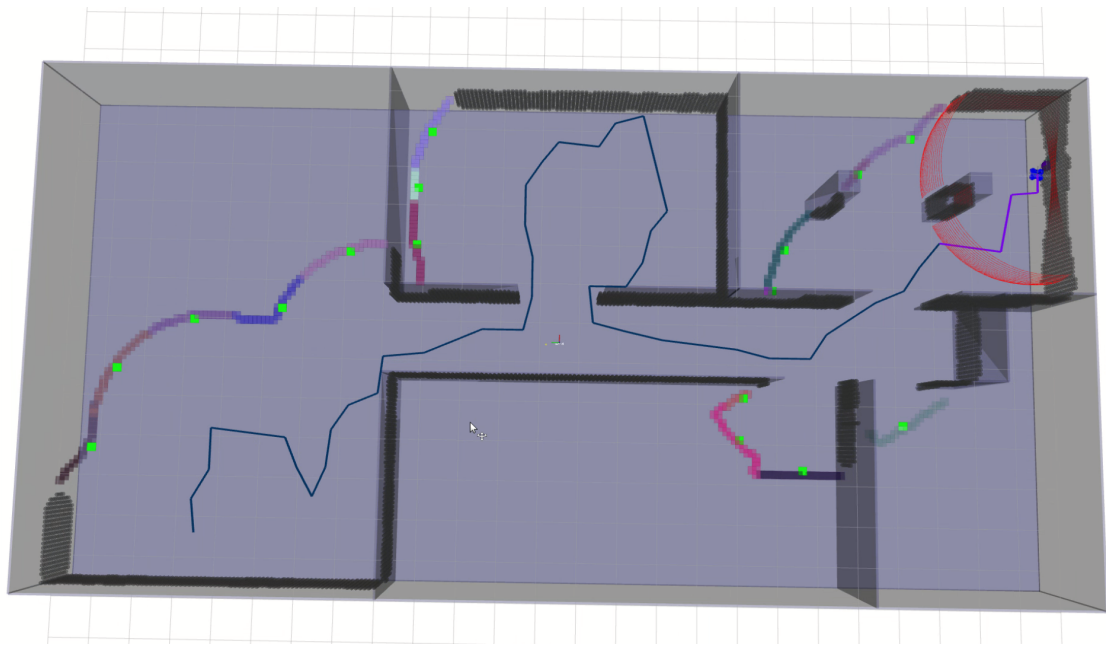


Figure 4.5: Representative trajectory for frontier exploration that is biased by the observed radiation gradient.

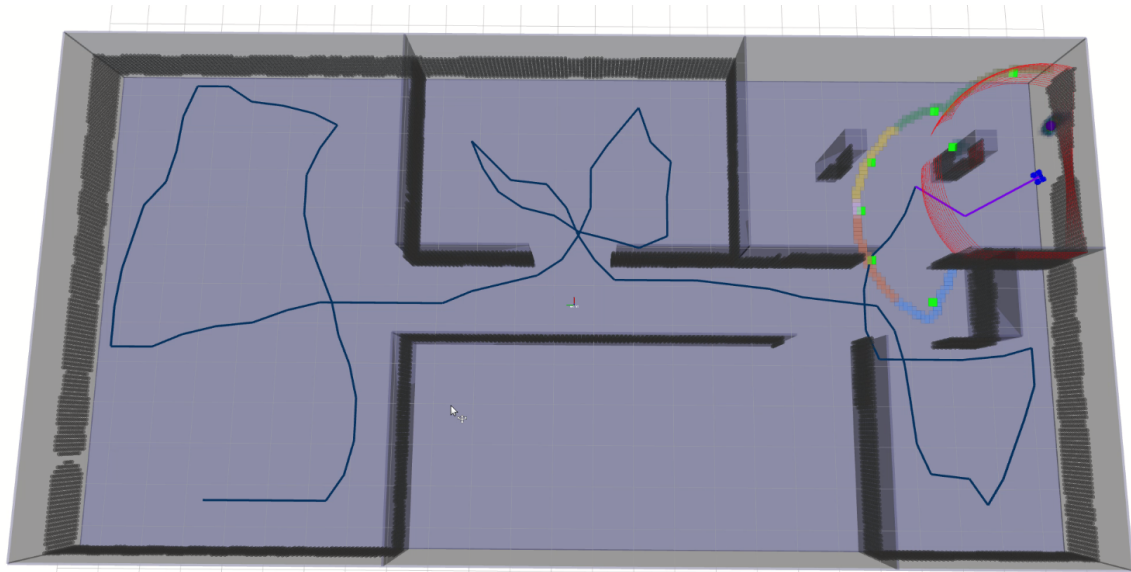


Figure 4.6: Representative trajectory for frontier exploration that is not biased by the observed radiation gradient.

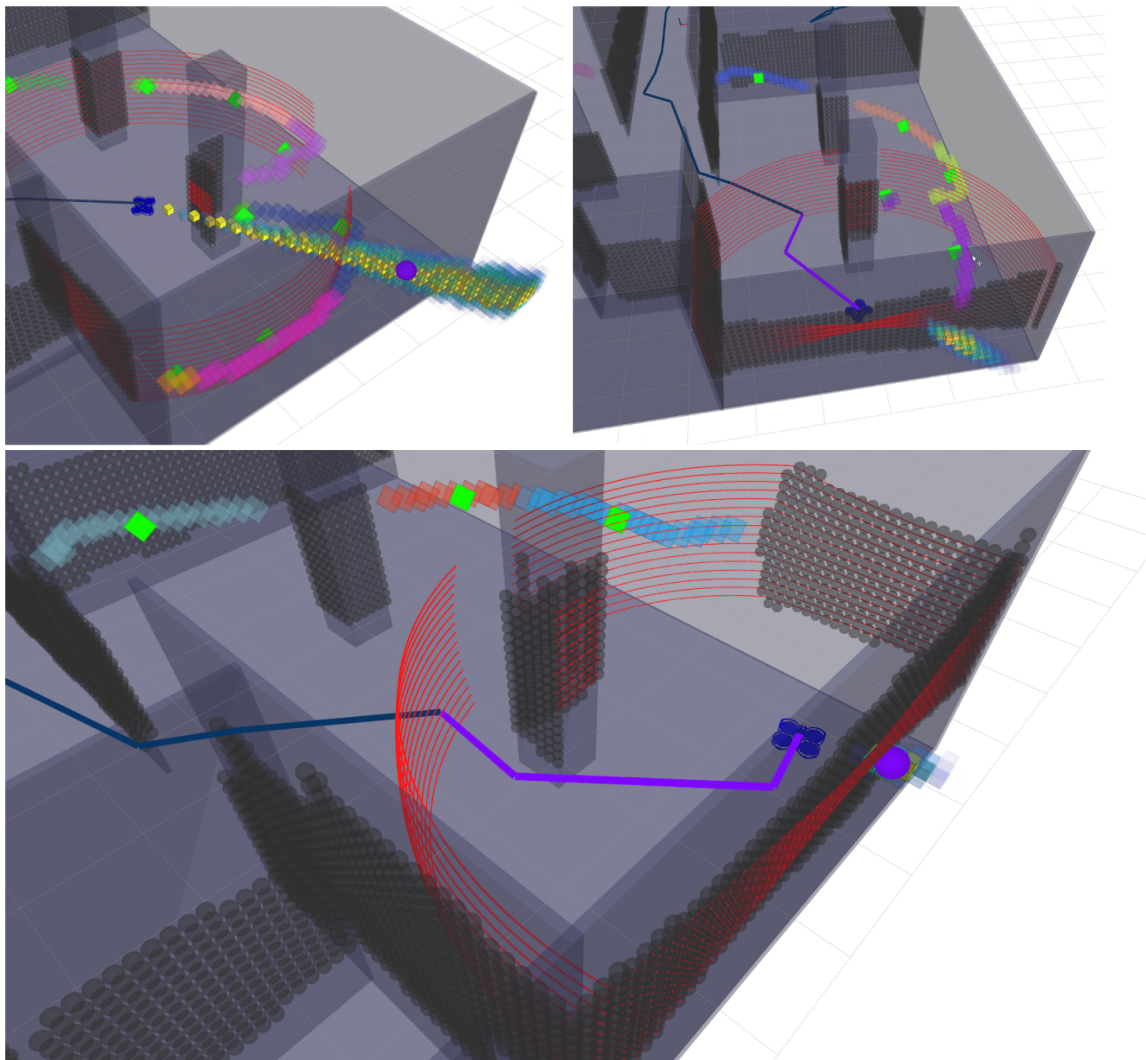


Figure 4.7: Progression of the source localization over multiple imaging dwells (clockwise from top left). The evolving radiation occupancy map that is used for the localization of the source (shown as the purple sphere) is shown as the blue and yellow voxels (in the order of increasing probability of radiation occupancy).

4.3.2 Multiple Source Localization

The FIM-optimal source localization trajectories developed in Chapter 4 were analyzed in an environment with clutter to restrict movement. This experiment sought to test the robustness of the combined exploration and source localization framework to localize a variety of sources of different strengths, isotopes, and locations. It was assumed that there was only one source of each isotope, such that the counts from the relevant energy lines of the localized sources could be discounted from the estimation of the gradient and count factors. To account for the lower strength sources used in this experiment, the transition between exploration and source localization phases was set to occur at 500 counts per second.

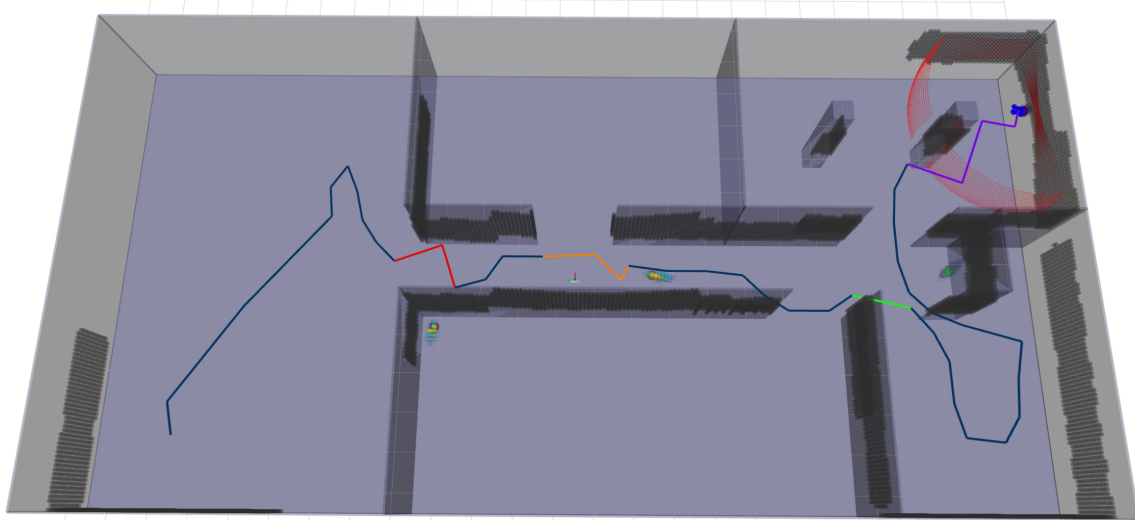


Figure 4.8: Representative frontier exploration and source localization trajectory for multiple sources.

Table 4.3: Multiple Source Exploration Results

Source (Strength)	Ba-133 (125 mCi)	Cs-137 (10 mCi)	Co-60 (10 mCi)	Na-22 (2 mCi)
Position (x, y, z), m	[−1.5, 3.5, 1.0]	[0.0, −2.0, 0.5]	[0.0, −9.5, 1.5]	[4.5, −12.0, 1.0]
Localization Error, m [$\mu \pm \sigma$]	0.14 ± 0.14	0.11 ± 0.12	0.05 ± 0.06	0.11 ± 0.08

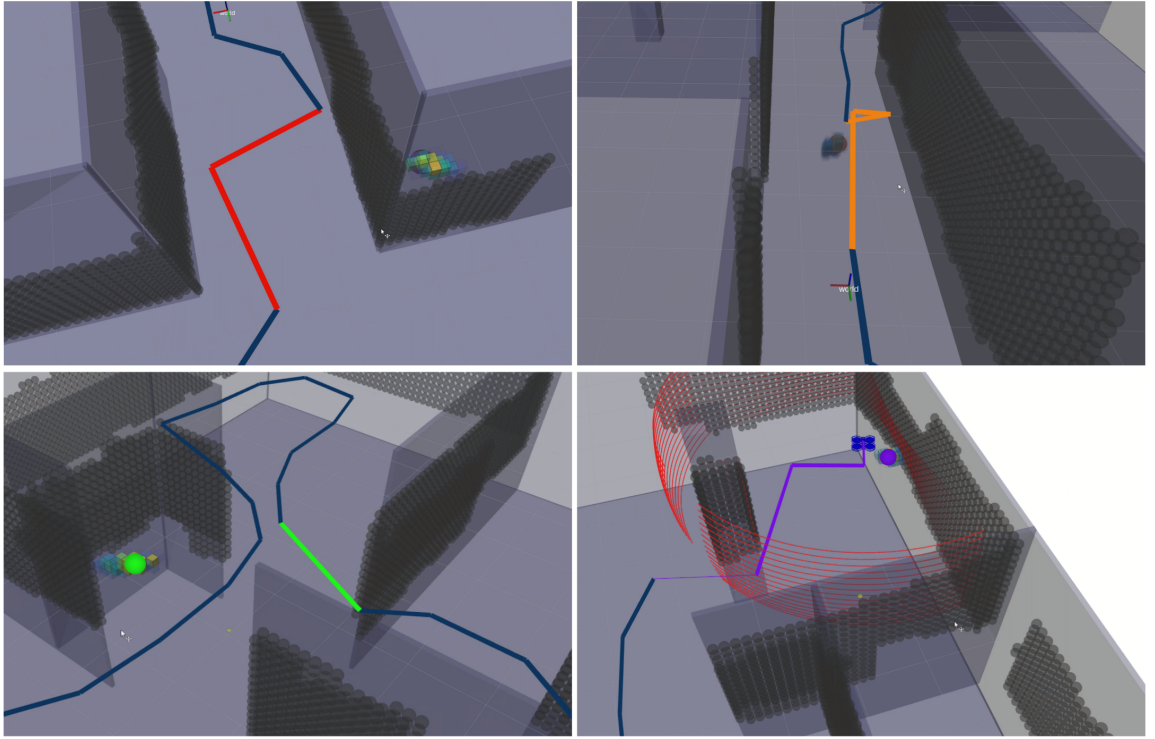


Figure 4.9: Close-up of the multiple sources placed in the environment and the trajectories taken by the robot to localize them (in corresponding colors)

The robot was able to successfully localize all four sources in all ten trials to within 15 cm on average, as recorded in Table 4.3. As Figure 4.8 shows, the trajectories taken to localize the sources (with corresponding colors) varied in shape and the number of dwells (which ranged from 2 to 5). Without sufficient space for a spiraling trajectory, a zig-zagging maneuver is favored that also decreases the distance to the source and obtains sufficient angular separation between measurements for triangulation. The localization of Ba-133 demonstrates how the camera is able to image through walls and effectively localize the source through triangulate without prior knowledge on the material and thickness of the wall or the source strength. Figure 4.9 shows the estimated locations of all four sources and the corresponding source localization trajectories of the trial shown in Figure 4.8.

Chapter 5

Conclusion

5.1 Discussion

In pursuit of a full exploration and radiation source localization framework for a gamma camera, this thesis first presents a method for mapping the spatial distribution of radiation using observations from this sensor. The first contribution of this work is the adaptation of the Maximum Likelihood Expectation Maximization (MLEM) radiation imaging algorithm into an radiation occupancy mapping framework. The proposed lightweight mapping implementation does not consider robot localization uncertainty as it was demonstrated in both simulation and in field tests to provide sufficient source localization accuracy. However, in challenging settings such as poorly illuminated, untextured, and symmetric environments, accurate source localization may require the integration of localization uncertainty into the map updates.

The subsequent chapters develop an exploration and active source localization framework that greedily selects frontiers and waypoints that minimize the time and distance to source localization. The framework is greedy and sequential in nature, toggling between exploration and source localization to localize one source at a time.

Though optimizing for the localization of multiple sources concurrently could lead to greater efficiency in theory, this work hypothesizes that the gain will often be marginal. The inverse square law of radiation attenuation causes a very rapid drop off of information away from a source such that sequentially approaching and localizing individual sources will generally be faster than trying to balance the localization of multiple sources along some contour. Shahidian et al. [44] aim to optimize the search path of two UAVs with respect to a number of radio frequency sources simultaneously. Their approach maximizes the determinant of the Fisher Information Matrix associated with the differential RSS readings acquired by the UAVs from every source. Unfortunately, their experiments do not provide great insight as their sources are clustered together and the resultant UAV trajectories only convey a general approach toward all the sources. More uniformly distributed sources could potentially draw out more interesting behavior from methods that aim to currently localize multiple sources, and confirm the gain or loss in efficiency.

The inverse square law attenuation of radiation is only one characteristic of the complex phenomenon of radiation propagation through matter. A gamma camera was used in this thesis as methods that rely solely on the observed counts often struggle to disambiguate between potential sensor, source, and environment configurations. Not only are count-based localization methods highly sensitive to assumptions on source strength and attenuation, the implementation of [17] in Chapter 2 revealed that it is also sensitive to roughly modeled sensor characteristics.

Bearing measurements provided by gamma cameras can be used to localize sources independent of strength or attenuation. Gamma cameras are also able to resolve independent directions for sources of the same isotope without any assumptions on the source count, provided that a sufficient number of photons are observed. However, like most methods, there are still a number of parameters to be tuned. When operating in

very large cluttered environments with only moderately strong sources, the imaging radius (i.e. the sensor footprint) of the gamma camera can be adjusted so that only the immediate neighborhood of the sensor is updated for computational efficiency. Additionally, the number of MLEM iterations run for imaging and the width of the energy window used both control the bias and variance of the source direction estimate provided by the radiation image. Lastly, the transition between the proposed frontier-based exploration and FIM-based source localization methods currently depends on an observed count rate threshold, which should be tuned to the expected source strengths, geometry, and attenuation of the environment. If it is set too low, then the imaging may begin far away from the source where imaging is costly and if it is set too high, then the robot will need navigate to a very close proximity to the source, which can be costly if there is a high amount of clutter surrounding the source.

5.2 Future Work

Effective use of a sensor or algorithm is often relies on context-dependent parameters and tuning, and the proposed exploration and source localization framework is no exception. However, characteristics of the environment, such as the material of the surrounding clutter, are not always observable. With partial information and complexity of forward simulating radiation propagation, it can be difficult to hand-design a good source localization policy for different classes of environments. For example, the proposed gradient-biased exploration framework will be increasingly less effective in environments with a very high degree of clutter and many local minima.

In such challenging environments, the cost of imaging from far away and obtaining an initial source location estimate for more informed exploration may outweigh the time likely to be spent in escaping local minima with a greedy algorithm. An interest-

ing direction of future work would thus be to learn a policy for knowing when to image during exploration. Partially observable Markov decision processes (POMDP) present a principled framework for decision making under uncertainty but often struggle to reason efficiently about very high dimensional spaces (e.g. the possible instantiations of a large map). Choudhury et al. [45] thus present an imitation learning framework for training policies that directly learn to imitate a clairvoyant oracle. An imaging policy trained under this framework could learn a mapping from a current state (e.g. the degree of clutter in the immediate neighborhood, observed gradient, observed counts, decision to image, etc) to expected time to source localization (provided by the oracle during train time).

Forward simulation of radiation propagation is not only computationally expensive but may be infeasible due to lack of necessary information. However, such forecasting is vital to informed decision making during source localization. The proposed approach for learning an imaging policy may begin a line of research that explores how learning-based methods can be leveraged to make a satisficing prediction of radiation propagation through acquired experience.

Appendix A

Appendix

A.1 Sensor Model for Gamma Camera

When using the photopeak assumption for two interaction events the sensor model is as follows [46]

$$o_{ij} = \frac{1}{d^2} e^{-\mu_{E_0_i} d_{1_{ij}}} \frac{d\sigma_c(E_{0_i}, E_{1_i})}{d\Omega} \frac{1}{d_{2_i} \sigma_{\theta_i} \sin(\theta_{e_i})} e^{-\frac{(\theta_{r_{ij}} - \theta_{e_i})^2}{2\sigma_{\theta_i}^2}} \dots \\ e^{-\mu_{E_0_i} - E_{1_i} d_{2_i}} \frac{\sigma_p(E_{2_i})}{\sqrt{2\pi(\sigma_{E_{1_i}}^2 + \sigma_{E_{2_i}}^2)}} e^{-\frac{(E_{0_i} - E_{1_i} - E_{2_i})^2}{2(\sigma_{E_{1_i}}^2 + \sigma_{E_{2_i}}^2)}} \quad (\text{A.1})$$

At a high level, $\frac{1}{d^2}$ accounts for the inverse square law dilution from the source voxel to the detector crystal, $e^{-\mu_{E_0_i} d_{1_{ij}}}$ is the probability for the photon to survive material attenuation from a particular voxel to the first interaction location in the CZT crystal, $\frac{d\sigma_c(E_{0_i}, E_{1_i})}{d\Omega}$ to Compton scatter at the first interaction location, $\frac{1}{d_{2_i} \sigma_{\theta_i} \sin(\theta_{e_i})}$ to go along the first direction along the Compton cone, $e^{-\frac{(\theta_{r_{ij}} - \theta_{e_i})^2}{2\sigma_{\theta_i}^2}}$ to have agreement between Compton cones based on deposited energies and the direction to a particular voxel, $e^{-\mu_{E_0_i} - E_{1_i} d_{2_i}}$ to survive material attenuation from the first interaction location

to the second interaction location, $\frac{\sigma_p(E_{2i})}{\sqrt{2\pi(\sigma_{E_{1i}}^2 + \sigma_{E_{2i}}^2)}}$ to be photoelectrically absorbed, and $e^{-\frac{(E_{0i} - E_{1i} - E_{2i})^2}{2(\sigma_{E_{1i}}^2 + \sigma_{E_{2i}}^2)}}$ to have agreement between the deposited energies and the actual incident energy. A similar form is used for three or more interaction events.

A.2 Maximum Likelihood Expectation Maximization

The analytical MLEM for list-mode data at the l th iteration is [46]

$$\hat{m}_{r_j}^{l+1} = \frac{\hat{n}_j}{s_j} = \frac{\hat{m}_{r_j}^l}{s_j} \sum_{i=1}^I \frac{o_{ij}}{\sum_{j'=1}^J o_{ij'} \hat{m}_{r_{j'}}^l} \quad (\text{A.2})$$

Conceptually, $\sum_{j'=1}^J o_{ij'} \hat{m}_{r_{j'}}^l$ is the likelihood of event i occurring, $\frac{\hat{m}_{r_j}^l o_{ij}}{\sum_{j'=1}^J o_{ij'} \hat{m}_{r_{j'}}^l}$ is the probability of event i occurring from a photon emitted from voxel j , and $\hat{n}_j = \sum_{i=1}^I \frac{\hat{m}_{r_j}^l o_{ij}}{\sum_{j'=1}^J o_{ij'} \hat{m}_{r_{j'}}^l}$ is the average number of detected photons from voxel j . $s_j = \sum_{i=1}^I o_{ij}$ is referred to as the sensitivity image, which is the probability that a photon emitted from voxel j is detected at all (this is related to the sensor geometry and source location). The sensitivity image will be set to obey the inverse square law. $\hat{m}_{r_j}^{l+1}$ is the average number of emitted photons from voxel j . The intuition behind this algorithm is captured by the statement $\hat{n}_{r_j}^l = \hat{m}_{r_j}^{l+1} s_j$, which says that the number of detected photons from voxel j , $\hat{n}_{r_j}^l$, is equal to the number of emitted photons from voxel j times the sensitivity of the detector to photons from that voxel. Acquiring \hat{n}_j^l constitutes the E step and acquiring $\hat{m}_{r_j}^{l+1}$ constitutes the M step.

At a high level, MLEM works in two phases. In the first phase, an analytical inverse sensor model [14] is developed from the first principles of photon interaction physics (e.g. considering attenuation, Compton scattering, photoelectric absorption,

etc). Given a set of observed interaction locations and energy depositions of an incident photon, the inverse sensor model assigns a probability to all possible directions of the photons origin.

In the second phase, MLEM iteratively estimates the maximum likelihood source distribution by jointly considering the inverse sensor model and the observed data in an expectation-maximization fashion. The expectation (E) step associates the incident photon of each observed event to the likely direction of origin using the current estimate of the source distribution in the environment. The maximization (M) step then uses the photon-direction association from the expectation step to compute the next maximum-likelihood estimate of the source distribution.

Bibliography

- [1] K. Hioki, “Estimation of Global Inventories of Radioactive Waste and Other Radioactive Materials,” tech. rep., International Atomic Energy Agency, Vienna, 2008.
- [2] D. Trimble, “Observations on Efforts by NNSA and the Office of Environmental Management to Manage and Oversee the Nuclear Security Enterprise,” tech. rep., US Government Accountability Office, Washington DC, 2016.
- [3] T. Yasutaka and W. Naito, “Assessing cost and effectiveness of radiation de-contamination in Fukushima Prefecture, Japan,” *Journal of Environmental Radioactivity*, vol. 151, no. January 2012, pp. 512–520, 2016.
- [4] D. Normile, “As evacuees move back, Fukushima cleanup faces daunting obstacles,” *Science*, March 2017.
- [5] Hanford Site, “Transuranic waste retrieval and certification,” 2017.
- [6] Createc, “N-visage gamma imager,” 2018.
- [7] K. Nagatani, S. Kiribayahi, Y. Okada, K. Otake, K. Yoshida, S. Tadokoro, T. Nishimura, T. Yoshida, E. Koyanagi, M. Fukushima, and S. Kawatsume, “Emergency Response to the Nuclear Accident at the Fukushima Daiichi Nu-

clear Power Plants using Mobile Rescue Robots,” *Journal of Field Robotics*, vol. 7, pp. 81–86, 2007.

- [8] M. Fackler, “Six Years After Fukushima, Robots Finally Find Reactors’ Melted Uranium Fuel,” November 2017.
- [9] G. F. Knoll, *Radiation Detection and Measurement*. John Wiley & Sons, 2010.
- [10] G. P. Glasgow, *Radiation Protection Instrumentation*. Wiley Online Library, 2006.
- [11] U. D. of Health and H. Services, “Toxicological profile for radon,” *Public Health Service*, 2012.
- [12] Mirion Technologies, “Types of Ionizing Radiation: Alpha, Beta, Gamma, X-Ray and Neutron Radiation,” 2018.
- [13] M. R. Morelande and A. Skvortsov, “Radiation field estimation using a Gaussian mixture,” in *International Conference on Information Fusion*, (Seattle, WA), pp. 2247–2254, 2009.
- [14] G. Minamoto, E. Takeuchi, and S. Tadokoro, “Estimation of ground surface radiation sources from dose map measured by moving dosimeter and 3D map,” *IEEE International Conference on Intelligent Robots and Systems*, 2014.
- [15] P. G. Martin, S. Kwong, N. T. Smith, Y. Yamashiki, O. D. Payton, F. S. Russell-Pavier, J. S. Fardoulis, D. A. Richards, and T. B. Scott, “3D unmanned aerial vehicle radiation mapping for assessing contaminant distribution and mobility,” *International Journal of Applied Earth Observation and Geoinformation*, vol. 52, pp. 12–19, 2016.

- [16] M. Morelande, B. Ristic, and A. Gunatilaka, “Detection and parameter estimation of multiple radioactive sources,” *International Conference on Information Fusion*, 2007.
- [17] J.-C. Chin, D. K. Y. Yau, and N. S. V. Rao, “Efficient and robust localization of multiple radiation sources in complex environments,” in *International Conference on Distributed Computing Systems*, pp. 780–789, IEEE.
- [18] J. Towler, B. Krawiec, and K. Kochersberger, “Terrain and Radiation Mapping in Post-Disaster Environments Using an Autonomous Helicopter,” *Remote Sensing*, vol. 4, no. 7, pp. 1995–2015, 2012.
- [19] A. A. R. Newaz, S. Jeong, H. Lee, H. Ryu, N. Y. Chong, and M. T. Mason, “Fast radiation mapping and multiple source localization using topographic contour map and incremental density estimation,” *IEEE International Conference on Robotics and Automation*, vol. 2016-June, pp. 1515–1521, 2016.
- [20] K. Vetter, R. Barnowksi, A. Haefner, T. H. Joshi, R. Pavlovsky, and B. J. Quiter, “Gamma-Ray imaging for nuclear security and safety: Towards 3-D gamma-ray vision,” *Nuclear Instruments and Methods in Physics Research, Section A: Accelerators, Spectrometers, Detectors and Associated Equipment*, vol. 878, pp. 159–168, 2018.
- [21] D. Xu, “Gamma-ray Imaging and Polarization Measurement using 3-D Position-sensitive CdZnTe Detectors,” 2006.
- [22] E. Nelson, “Berkeley Localization and Mapping,” 2015.

- [23] J. M. Passerieux and D. Van Cappel, “Optimal observer maneuver for bearings-only tracking,” *Bayesian Bounds for Parameter Estimation and Nonlinear Filtering/Tracking*, vol. 34, no. 3, pp. 761–772, 2007.
- [24] S. E. Hammel, “Optimal Observer Motion for Bearings-only Localization and Tracking,” 1998.
- [25] S. S. Ponda, R. M. Kolacinski, and E. Frazzoli, “Trajectory Optimization for Target Localization Using Small Unmanned Aerial Vehicles,” in *AIAA Guidance, Navigation, and Control Conference*, 2009.
- [26] J. Le Cadre, “Optimization of the observer motion for bearings-only target motion analysis,” in *IEEE Conference on Decision and Control*, vol. 4, pp. 3126–3131, IEEE, 1997.
- [27] A. N. Bishop and P. N. Pathirana, *Optimal Trajectories for Homing Navigation with Bearing Measurements*, vol. 41. IFAC, 2008.
- [28] Y. Bar-Shalom, X. R. Li, and T. Kirubarajan, *Estimation with Applications to Tracking and Navigation: Theory, Algorithms, and Software*. John Wiley & Sons, 2004.
- [29] B. Bayat, N. Crasta, H. Li, and A. Ijspeert, “Optimal search strategies for pollutant source localization,” *2016 IEEE/RSJ International Conference on Intelligent Robots and Systems (IROS)*, pp. 1801–1807, 2016.
- [30] G. Ferri, A. Munafò, R. Goldhahn, and K. LePage, “A non-myopic, receding horizon control strategy for an auv to track an underwater target in a bistatic sonar scenario,” in *IEEE Conference on Decision and Control (CDC)*, pp. 5352–5358, IEEE, 2014.

- [31] A. Ryan and J. K. Hedrick, “Particle filter based information-theoretic active sensing,” *Robotics and Autonomous Systems*, vol. 58, no. 5, pp. 574–584, 2010.
- [32] F. Koohifar, A. Kumbhar, and I. Guvenc, “Receding horizon multi-uav cooperative tracking of moving rf source,” *IEEE Communications Letters*, vol. 21, no. 6, pp. 1433–1436, 2017.
- [33] B. Charrow, N. Michael, and V. Kumar, “Active Control Strategies for Discovering and Localizing Devices with Range-Only Sensors,” in *Algorithmic Foundations of Robotics*, 2015.
- [34] J. Tisdale, Z. Kim, and J. K. Hedrick, “Autonomous UAV Path Planning and Estimation,” pp. 35–42, 2009.
- [35] N. Atanasov, J. Le Ny, N. Michael, and G. J. Pappas, “Stochastic source seeking in complex environments,” in *IEEE International Conference on Robotics and Automation (ICRA)*, pp. 3013–3018, IEEE, 2012.
- [36] H. Kushner and G. G. Yin, *Stochastic approximation and recursive algorithms and applications*, vol. 35. Springer Science & Business Media, 2003.
- [37] J. C. Spall, *Introduction to stochastic search and optimization: estimation, simulation, and control*, vol. 65. John Wiley & Sons, 2005.
- [38] B. Williams and Z. He, “Evaluation of Compton Imaging Efficiency Degradation Factors in Large Volume, Pixelated CdZnTe Sensors,” *2017 IEEE Nuclear Science Symposium and Medical Imaging Conference*, pp. 1–5.
- [39] B. Yamauchi, “A frontier-based approach for autonomous exploration,” in *IEEE International Symposium on Computational Intelligence in Robotics and Automation*, pp. 146–151, IEEE, 1997.

- [40] T. Cieslewski, E. Kaufmann, and D. Scaramuzza, “Rapid exploration with multi-rotors: A frontier selection method for high speed flight,” in *IEEE/RSJ International Conference on Intelligent Robots and Systems (IROS)*, pp. 2135–2142, IEEE, 2017.
- [41] B. Tovar, L. Muñoz-Gómez, R. Murrieta-Cid, M. Alencastre-Miranda, R. Monroy, and S. Hutchinson, “Planning exploration strategies for simultaneous localization and mapping,” *Robotics and Autonomous Systems*, vol. 54, no. 4, pp. 314–331, 2006.
- [42] H. H. González-Banos and J.-C. Latombe, “Navigation strategies for exploring indoor environments,” *The International Journal of Robotics Research*, vol. 21, no. 10-11, pp. 829–848, 2002.
- [43] J. N. Twigg, J. R. Fink, L. Y. Paul, and B. M. Sadler, “Rss gradient-assisted frontier exploration and radio source localization,” in *IEEE International Conference on Robotics and Automation (ICRA)*, pp. 889–895, IEEE, 2012.
- [44] S. A. A. Shahidian and H. Soltanizadeh, “Optimal trajectories for two uavs in localization of multiple rf sources,” *Transactions of the Institute of Measurement and Control*, vol. 38, no. 8, pp. 908–916, 2016.
- [45] S. Choudhury, A. Kapoor, G. Ranade, and D. Dey, “Learning to gather information via imitation,” in *IEEE International Conference on Robotics and Automation (ICRA)*, pp. 908–915, IEEE, 2017.
- [46] C. G. Wahl, *Imaging, detection, and identification algorithms for position-sensitive gamma-ray detectors*. PhD thesis, University of Michigan, 2011.